Corresponding Author Email: kumar176103003@iitg.ac.in

Numerical investigation of Magnetic Pulse Welding of D9 Steel Tube to SS316LN End Plug using Lagrangian Finite Element and Smoothed Particle Hydrodynamics (SPH) and its Experimental Validation

M. R. Kulkarni [1], Deepak Kumar [2, *], Tanmay Kolge [1] , Arup Nandy [2], Sachin D. Kore [3], R. I. Bakhtsingh [1]

[1]Accelerator and Pulse Power Division, BTDG, Bhabha Atomic Research Centre, Mumbai, India

[2]Department of Mechanical Engineering, IIT Guwahati, Assam, India

[3] School of Mechanical Sciences, Indian Institute of Technology Goa, India

[*] Corresponding Author Email: kumar176103003@iitg.ac.in

Preprint

Abstract

Conventional mesh-based numerical methodologies cannot accurately simulate high-speed impact welding due to extreme distortion of mesh. Therefore, a smoothed particle hydrodynamics (SPH) based methodology is implemented to study the welding morphology and jetting phenomenon during magnetic pulse welding (MPW) of D9 clad tubes and SS 316LN end plugs after carrying out electromagnetic and structural deformation analysis using Lagrangian Finite element method. Different experimental parameters like taper angle, taper length, stand-off distance and discharge energies are varied to minimise leak-tightness. Discharge voltage of 17 kV and 18 kV and taper angle of 8 degrees is observed to be best suited during the experiment. Simulation results are validated with experimental observations.
Furthermore, the joints are tested with the help of various non-destructive and destructive techniques. Uniformity at the joint interface is established by X-ray computer tomography. Moreover, the hydraulic pressure burst test shows failure in the unwelded region at the burst pressure of 105 MPa. Therefore, the current work discusses the applicability of the MPW technique as an alternative method to create a D9 tube to SS 316 LN end plug for a fast breeder reactor and the SPH technique on successfully reproducing experimentally observed interface morphology.

1. Introduction

The fuel clad end-plug (widely used for reactor fuel pins) fabrication is normally done using the traditional fusion welding approach [1, 2, 3]. Traditional procedures such as gas tungsten arc welding (GTAW) are preferred to link clad tubes to the end plugs. However, these

Corresponding Author Email: kumar176103003@iitg.ac.in

techniques have high heat input, resulting in a larger heat-affected zone (HAZ). As a result, methods like laser welding having higher energy density have exhibited greater process control and smaller HAZ as an alternative to GTAW [3, 4]. Compared to thermal nuclear reactors, the materials must function at greater temperatures and in a harsher radiation environment to be employed in sodium-cooled fast reactors [5]. As a result, the outer tube material is titanium modified SS316, known as alloy D9 (15 percent Cr-15 percent Ni-0.2 percent Ti). However, due to the production of low melting point eutectics caused by impurities such as sulphur and phosphorous, fusion welding of austenitic stainless steel (ASS) causes hot cracking flaws [6, 7]. When phosphorous is specified as an alloying element, the defect rises, but the maximum sulphur concentration is limited to 0.0005 wt. percent in modified alloys. The Ti proportion of D9 steel makes ASS more prone to breaking [1]. Hot cracking tests in 316LN ASS have revealed that the total concentration of P and S must be kept below 0.03 wt% to avoid the negative effects of their segregation [1, 8, 9]. Noh et al. [10] discuss the traditional welding process causing residual stress and microstructural heterogeneity leading to brittle fracture and embrittlement. A solid-state welding procedure can eliminate such problems when attaching a fuel clad tube to an end-plug in a fuel pin assembly. Magnetic pulse welding (MPW) is a solid-state welding technology that produces connections devoid of heat impacted zones and hot fractures [11, 12]. It is appropriate for axis-symmetric components. It is a high-speed or impulse forming technique that employs a transient alternating magnetic field to strike non-contact forces on a conductive working piece without using working material. No filler material is utilised, and the contact-free force causes nearly minimal damage to the workpiece's surface [13, 14]. It is also one of the industry's most extensively utilised high energy rate forming (HERF) processes [15, 16]. MPW of copper-brass tube-to-rod connections is explored by Faes et al. [17], and the authors have inspected a weldability window along with air leak tightness of the produced sample. The authors further establish that the thickness of the interfacial layer is affected by the stand-off distance and discharge energy. Cui et al. [18] have investigated the aluminium-steel tubular joining using MPW and established a critical thickness of the outer workpiece dependent on the input parameter. A value less than the critical thickness causes tube separation during tensile testing, whereas a value greater than the critical thickness causes parent tube failure, resulting in increased joint strength. Mishra et al. [19] have designed a 40 kJ MPW setup to study a weldability window for joining using magnetic pulse expansion forming of Al6061 tube, and the authors discover the necessity of higher discharge energy in the case of thicker tubes compared to thinner tube. Furthermore, an analytical and experimental evaluation during MPW of a thin-walled tube is performed by Leug-Althoff et al. [20], and the authors have studied the deformation behaviour during the welding process using inline laser-based measurement technology. The authors have also observed improved weld quality by using a reusable mandrel to support the inner tube. Yu et al. [13] created aluminium-mild steel composite tubes using the magnetic pulse cladding process, and the authors discuss how cladding quality gets affected by the shape of the field shaper in the working zone and develops an optimised geometry. Shotri et al. [21] have proposed an analytical methodology for estimation of impact velocity along with validation of results with experimentally observed values which assists in designing MPW experiments. Numerous

Preprint

Corresponding Author Email: kumar176103003@iitg.ac.in

destructive and non-destructive tests have demonstrated the longevity and integrity of MPW joints [22], and this technique may be used in various large-scale sectors, including automobile, aerospace, electrical, ordnance and packaging [16]. Furthermore, fuel pin cladding tubes in reactors are used directly for tube-to-end plug joints [22]. Impact welds have a wave-like (waviness) weld interface, which is a commonly used indicator for optimised process parameters or good weld formation [23]. However, the shape of waviness varies depending on the material combination [24]. Previous research has looked at the effects of material thickness on interfacial morphology. The wavelength is governed by the interference of stress waves at the contact, according to Godunov et al. [25] and Blazynski [24]. Lee et al. [26] used experimental approaches as well as arbitrary–lagrangian–eulerian (ALE) simulations to investigate the influence of flyer thickness on the interface. To keep the impact velocity and angle constant while modifying the flyer thickness, the authors have employed direct velocity measurements and pre-set collision angles. The interfacial wavelength rises with the thickness of the aluminium flyer, implying that stress wave interference at the weld interface plays a role in wave development. Jaramillo et al. [27] (for explosive welding (EXW)) and Ben-Artzy et al. [28] (for axisymmetric MPW) have conducted experimental tests by altering the target thickness. Although, despite of similar hypotheses, their results are observed to be contradictory. Both experiments have found that as the target thickness to flyer thickness ratio increases, the wavelength of the interfacial waviness morphology increases. However, Jaramillo et al. have observed stagnation of change in interfacial waviness values once the ratio exceeds 2. The numerical analysis provides flexibility in selecting welding parameters (collision velocity, collision angle, meta; combination and shape of the workpiece) to study. The study is usually performed using the Lagrangian or Eulerian methods. The phenomena of wavy interface creation and metal jet emission, on the other hand, are difficult to replicate. Kakizaki et al. [29] have explained that those numerical approaches cannot cope with severe deformation at the collision contact and need a very small mesh size to recreate the exact morphological change at the interface. Therefore, meshless approaches such as smoothed particle hydrodynamics (SPH), in which particles are specified as interpolated points of physical quantities, and each particle travels without deforming itself during analysis, can be beneficial according to Jiedi et al. [30]. Sarvari et al. [31] have examined at how varying welding gaps affected the morphology of MPW joints and collision surfaces. The authors have achieved metallurgical bonding of Cu and Al sheets with a 0.7 mm welding gap. When the distance is wider, the welding fails owing to excessive impact energy. These researches have aided the advancement of MPW technology. However, the study around metal jet process, which is the core of MPW [32], is still insufficient. The majority of studies focus on residue characterization and simulation research [33]. As a result, more research into the metal jet formation process and properties is required. This paper performs a numerical and experimental investigation of magnetic pulse welding of D9 steel tube to SS316LN end plug. An axisymmetric Lagrangian (mesh-based) simulation model is developed and validated with experimentally observed deformation value. An SPH (meshless) simulation model is also developed, and simulated interface morphology is compared with experimentally obtained microstructural morphology. To find the weldability window, SPH simulations are performed

Preprint

Corresponding Author Email: kumar176103003@iitg.ac.in

for different contact angles and contact velocity. Furthermore, helium burst test and argon gas pressure burst test at varying temperatures are also performed to establish the durability of the D9-SS 316LN tube-to-end plug sample. SEM analyses the interface morphology and the welding quality.

2. Working principle

A capacitor bank is employed as a power supply in the case of MPW. After charging the capacitor bank, it is discharged to an instantaneous discharge energy into a coil in a very short period of time (10 μs- 30 μs). This results in the flow of a damped sinusoidal current in the coil and the formation of a magnetic field according to Lenz's law. According to Faraday's law of electromagnetic induction, the magnetic field induces an eddy current in the opposite direction of the primary current on the surface of the nearby conductor. The induced current creates the magnetic field. The Lorentz force due to the combined effect of two opposing magnetic fields, provides magnetic pressure to the workpiece, causing plastic deformation and accelerating the outer workpiece (flyer workpiece) to a high enough speed. When the flyer workpiece collides with the target (inner) workpiece, a weld is formed between the flyer and the target tube if favourable impact angle and velocity are. A metallic bond is established when the distance between two workpieces' atoms is lower than their attractive mutual force range [34-35]. The entire procedure is quick, taking approximately 10-30 μs [10].
Furthermore, because the electrical conductivity of the D9 steel outer tube is poor in this case, an outer Cu driver tube is utilised to aid the electromagnetic welding process by providing required Lorentz force. Cu has been chosen as a driving tube because of its low yielding stress and good electrical conductivity. Due to the contact between the driver and flyer tubes, Lorentz force operates on the driver tube, which is mechanically transmitted to the flyer tube, and if the equivalent stress operating on the driver and flyer tubes exceeds their yield stress, both tubes begin to deform simultaneously.

3. Physics in the process

The electromagnetic process is governed by Maxwell's equation.

$$\vec{\nabla} \times \vec{E} = \frac{-d\vec{B}}{dt}, \tag{1}$$

where $\vec{E}$ and $\vec{B}$ are the electric field intensity and magnetic flux density, respectively, and t is the time.

$$\vec{\nabla} \times \vec{H} = \vec{J} + \varepsilon \frac{d\vec{E}}{dt}, \tag{2}$$

Preprint

Corresponding Author Email: kumar176103003@iitg.ac.in

where $\vec{H}$ and $\vec{J}$ represents the magnetic field intensity and total current density, respectively and, ε is electrical permittivity.

$$\vec{\nabla} \cdot \vec{B} = 0\,, \tag{3}$$

$$\vec{\nabla} \cdot \vec{E} = \frac{\rho}{\varepsilon}\,, \tag{4}$$

where ρ represents total charge density

$$\vec{J} = \sigma\vec{E} + \vec{J}_S, \tag{5}$$

while $\vec{J}_S$ is the current source density, σ is electrical conductivity. From Eq. (3) magnetic flux density can be written as:

$$\vec{B} = \vec{\nabla} \cdot \vec{A}, \tag{6}$$

where $\vec{A}$ is the vector potential. Using Eq. (6), the induced total current density $\vec{J}$ over the workpiece can be expressed by Eq. (7) and (8).

$$\vec{J} = \vec{\nabla} \times \frac{\vec{B}}{\mu_{\mathrm{m}}}, \tag{7}$$

$$\vec{J} = \vec{\nabla} \times \frac{1}{\mu_{\mathrm{m}}}\left(\vec{\nabla} \times \vec{A}\right), \tag{8}$$

where μ_{m} is the magnetic permeability of the medium. According to Maxwell's equation, the Lorentz force, which acts on the workpiece as a body force, $\vec{F}$ can be calculated by

$$\vec{F} = \vec{J} \times \vec{B} = \left(\vec{\nabla} \times \frac{\vec{B}}{\mu_{\mathrm{m}}}\right) \times \vec{B} \tag{9}$$

The Lorentz force $\vec{F}$ can be used to determine magnetic pressure p by integrating the body force over the thickness of the tube.

$$p(r,t) = \int_{ro}^{ri} F(r,t)dr = \frac{1}{2}\mu\left(H_{\mathrm{gap}}^2(t) - H_{\mathrm{pen}}^2(t)\right) \tag{10}$$

When the depth of the skin is less than the thickness, the infiltrated magnetic field may be ignored, and magnetic pressure is dictated by the thickness.

$$p(t) = \frac{1}{2}\mu H_{\mathrm{gap}}^2(t) \tag{11}$$

Preprint

Corresponding Author Email: kumar176103003@iitg.ac.in

4. Numerical Simulation Setup with Finite Element Lagrangian Model and Smoothed Particle Hydrodynamics (SPH)

Authors have simulated Magnetic Pulse Welding using Lagrangian finite element analysis and smoothed particle hydrodynamics. Combining the ANSYS Maxwell and ANSYS explicit dynamics software programmes, a non-coupled finite element model is simulated. The simulation divides the magnetic pulse welding problem into two parts (electromagnetic and mechanical). ANSYS Maxwell and ANSYS explicit dynamics solves the electromagnetic and mechanical part respectively, as shown in Fig. 1. Dimensions of the various magnetic pulse welding setup components are shown in Fig 2. After that, we have used Smoothed Particle Hydrodynamics (SPH) in ANSYS Autodyne (Fig. 1) for successful numerical modelling of metal jet emission and interface welding morphology.

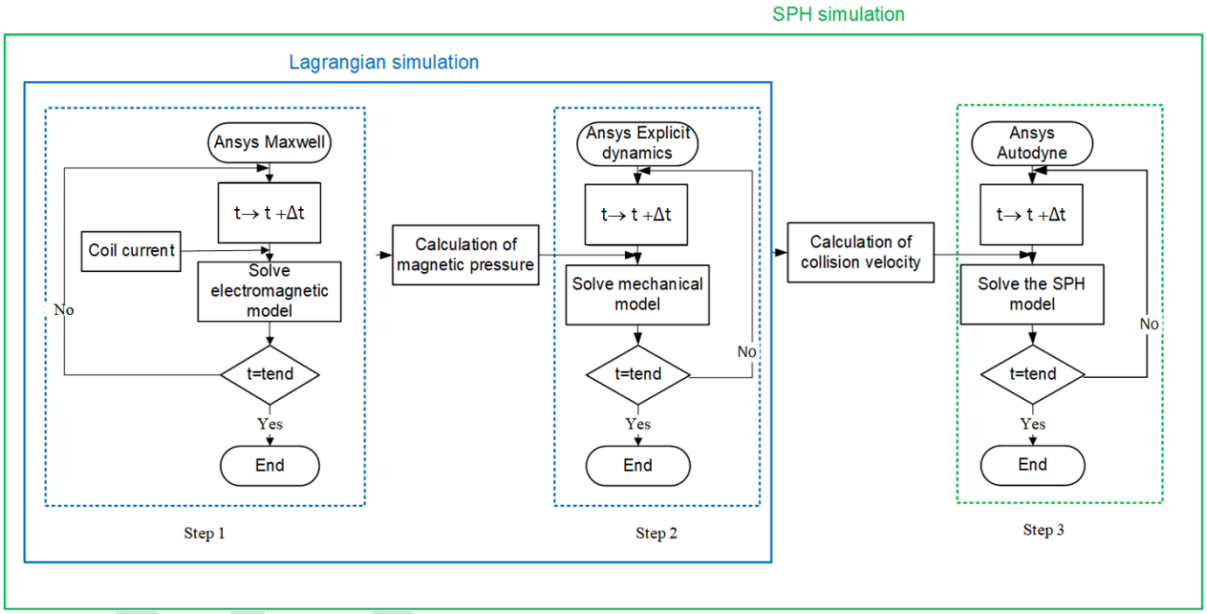

Fig. 1 Brief Flow Chart for Numerical Modelling for Electromagnetic analysis (ANSYS Maxwell), Structural deformation (ANSYS Explicit dynamics) and Welding morphology (ANSYS Autodyne)

Corresponding Author Email: kumar176103003@iitg.ac.in

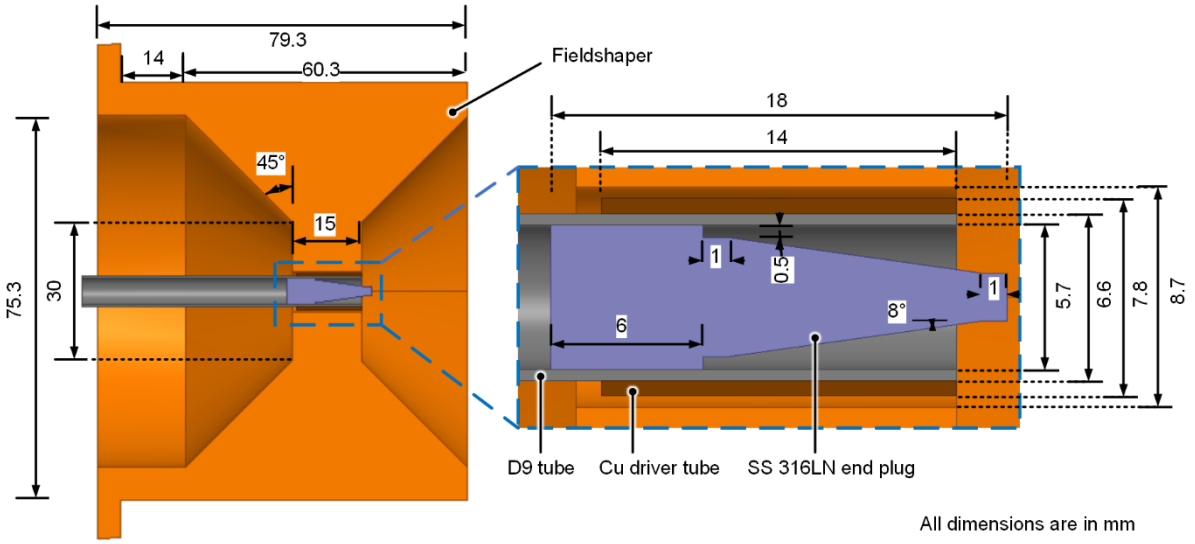

Fig. 2 Dimensions of various parts of the components of the magnetic pulse welding setup

4.1. Electromagnetic analysis using ANSYS Maxwell

During experiments, current is monitored using an oscilloscope and utilised as an input to the ANSYS Maxwell to compute the magnetic field. Fig. 3 (a) shows the input current curves. The coil, driver tube, flyer tube, end plug, and field shaper are all enclosed in air in a three-dimensional electromagnetic field model (Fig. 3 (b)). As previously stated, the coil has a ring current load that provides a magnetic field for MPW. A vacuum box is assumed to be surrounding the coil-tube model in such a way that its dimension is sufficient enough for magnetic field to decrease to zero in the far-field. The coil, driver tube, flyer tube, end plug and field-shaper are meshed into a hexahedral mesh model, as shown in Fig. 3(c). Fig. 3 (d) shows the current density of unduced current for Cu driver tube at 15 µs. An induced current is observed on the outer surface of driver tube in the working zone of the field shaper. However, outside the workingzone, lower current density is observed. The magnetic field at the surface of the Cu driver tube is obtained to calculate the magnetic pressure, which is further to calculate structural deformation in the ANSYS explicit dynamics

Preprint

Corresponding Author Email: kumar176103003@iitg.ac.in

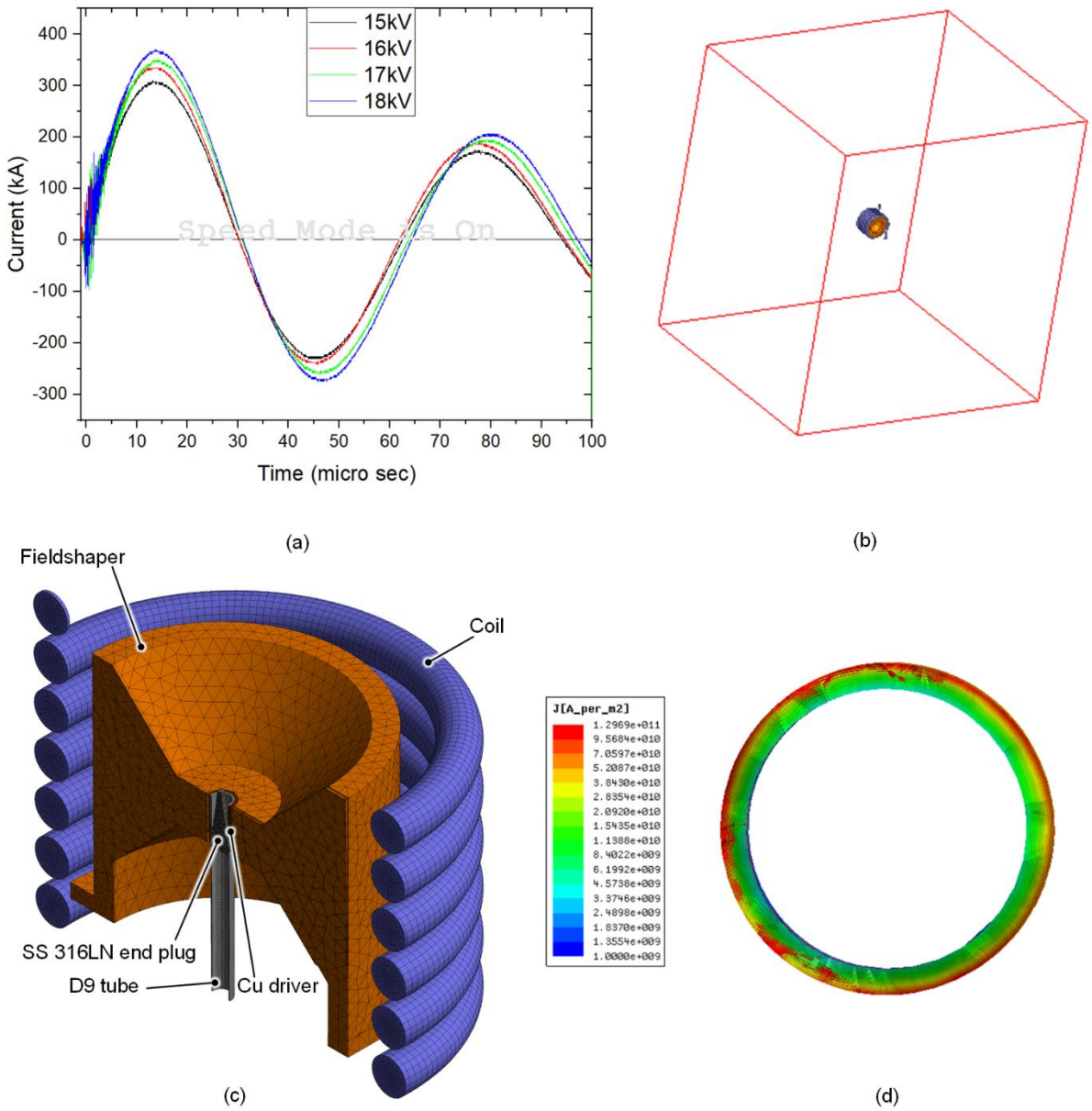

Fig. 3 Simulation model for electromagnetic field analysis (a) current curve, (b) ANSYS Maxwell model, (c) grid details showing the sectional view and (d) current density for 18 kV at 15 µs showing induced current at the Cu driver tube surface in the middle of the working zone

4.2. Structural deformation analysis using ANSYS Explicit Dynamics

ANSYS Explicit Dynamics is a multi-physics software capable of solving short-duration, structural problems with complex contact interactions with or without friction, including linear and non-linear buckling, fracture, fatigue and more. The problems may have nonlinearities in the geometry, such as large deformation and considerable strain, including rate-independent and rate-dependent plasticity. They make use of both linear and non-linear material models. Structural analysis having very small-time steps, such as high-speed impacts or explosions, can

Corresponding Author Email: kumar176103003@iitg.ac.in

be performed efficiently using the Explicit Dynamics package. The physical problem domain, boundary conditions and loading are axisymmetric. Therefore, an axisymmetric simulation model is used for the mechanical part instead of a 3-D model to save time and cost. The conversion of a 3-D model into an axisymmetric model is shown in Fig. 4. The ANSYS explicit dynamics model schematic is shown in Fig. 4 (b). The linear meshing technique is used.

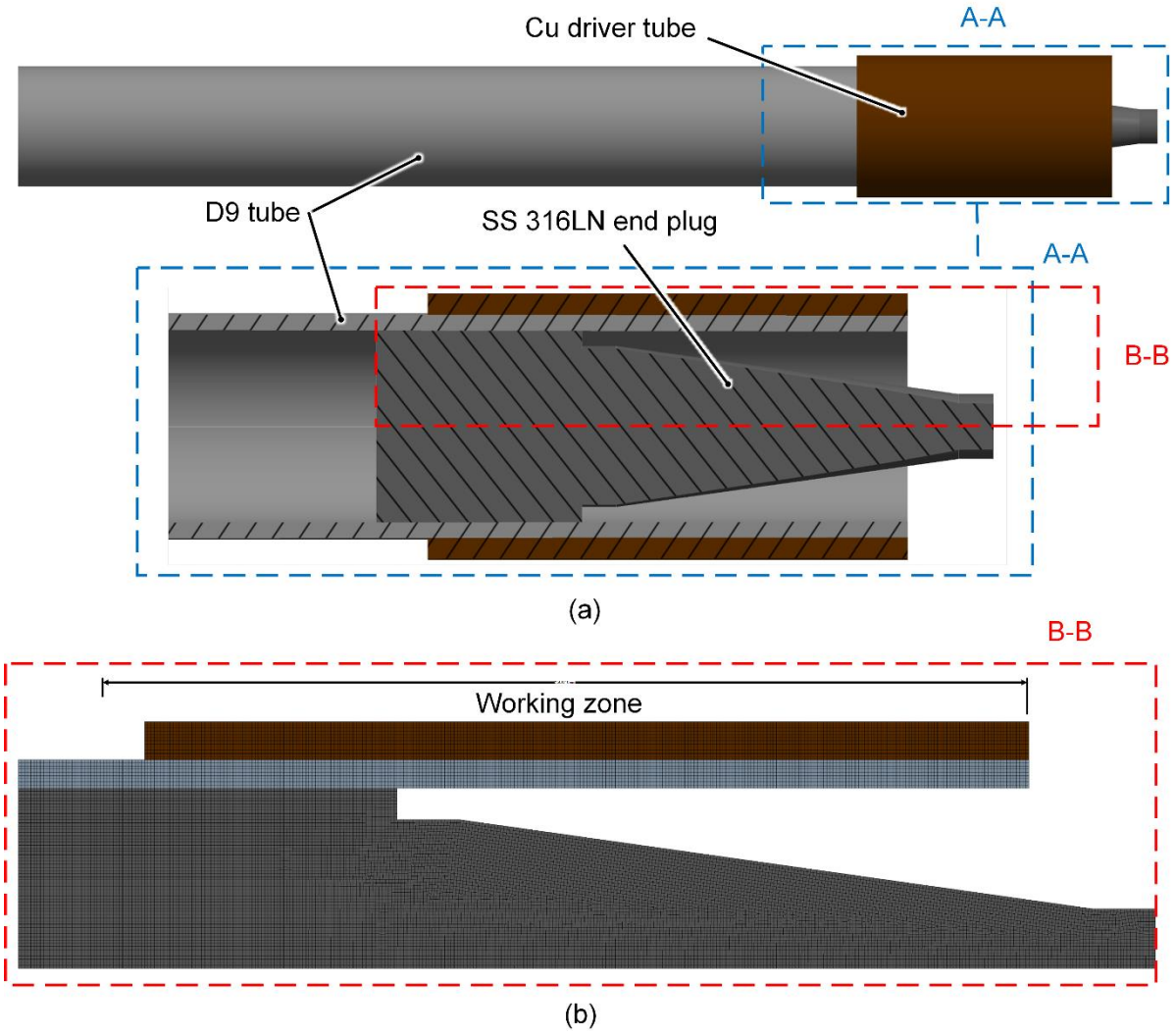

Fig. 4 (a) 3-D model showcasing the arrangement of components and (b) Axisymmetric meshed simulation model for ANSYS explicit dynamics

The ends of the tubes and end plug are fixed using boundary conditions in ANSYS to replicate the experimental setup. The pressure data obtained from ANSYS Maxwell is used here as input. Convergence analysis has been done to determine the optimum mesh size and time step. The Johnson-Cook (J-C) material model is used for all the workpiece material, a recommended material model for high temperature and high strain-rate processes [36]. J-C model can be described as:

Corresponding Author Email: kumar176103003@iitg.ac.in

$$\sigma_y = (A + B\varepsilon^n)\left(1 + C\, ln\left(\frac{\dot{\varepsilon}}{\dot{\varepsilon}_o}\right)\right)\left(1 - \left(\frac{T - T_r}{T_m - T_r}\right)^m\right), \quad (12)$$

where, σ_y represents equivalent plastic stress. ε, $\dot{\varepsilon}$ and $\dot{\varepsilon}_0$ represents equivalent plastic strain, equivalent plastic strain rate and reference equivalent plastic strain rate, respectively. *A*, *B*, *C*, *n* and *m* are material constants, whereas *T*, T_r and T_m represent absolute temperature, room temperature and melting temperature, respectively. Parameters of the J-C material model for Cu, D9 and SS 316LN are shown in Table 1. [37,38]. Properties of the materials are considered to be isotropic for this simulation. The shock wave equation of state (EOS) is defined in the J-C material model to construct the pressure-volume relationship during shock compression of solid analysis. Linear polynomial EOS used in the J-C material model can be described as

$$P = c_o + c_1\mu + c_2\mu^2 + c_3\mu^3 + E_o(c_4 + c_5\mu + c_6\mu^2), \quad (13)$$

where *P* denotes pressure, c_o, c_1, c_2, c_3, c_6, c_4, c_5 and c_6 are the constants of EOS, $\mu = \frac{\rho}{\rho_0} - 1$ denotes compression factor where $\frac{\rho}{\rho_0}$ being the ratio of current density to the initial density and E_o represents specific internal energy. Constants of EOS for copper are shown in Table 2.

Table 1 Constants of J-C material model for Cu, D9 and SS 316LN [37, 38]

Material	A(MPa)	B(MPa)	n	C	T_m(K)	m
Copper	90	292	0.31	0.025	1331	1.09
D9	120	465	0.308	0.1	1449	0.75
SS 316LN	250	1143	0.67	0.0229	1440	1

Table 2 Constants of linear polynomial EOS of copper [39]

Materials	c_o	c_1(N/m^2)	c_2(N/m^2)	c_3	c_4	c_5	c_6	E_o
Copper	0	140×10^9	2.8×10^9	1.96	0.47	0	0	0

Preprint

4.3. Fluid dynamics modelling of Welding morphology using Smoothed Particle Hydrodynamics in ANSYS Autodyne

Corresponding Author Email: kumar176103003@iitg.ac.in

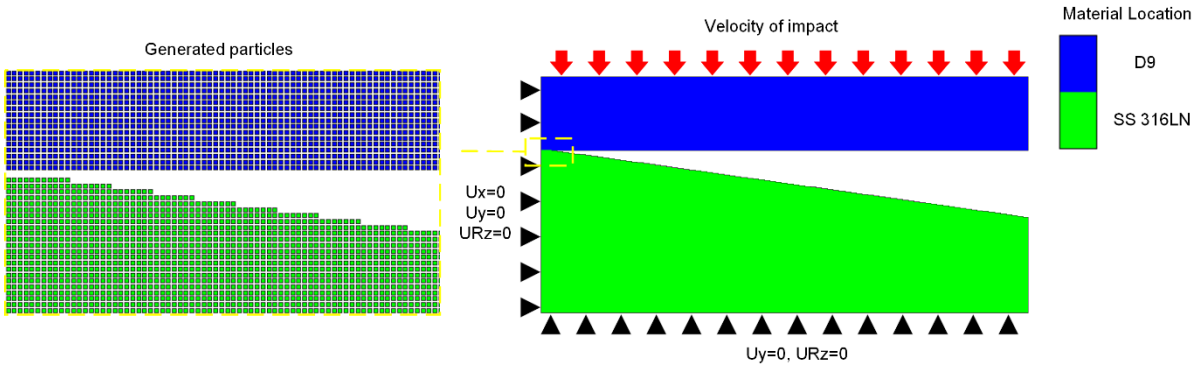

Fig. 5 Geometry used for the SPH numerical model

SPH is a meshless approach in which a group of particles with a spatial position represent a continuous body. Relative attributes of neighbouring particles are summed up to calculate the physical attributes of individual particles. The smoothing length and number of neighbouring particles are determined by the kernel function, also known as the weighting function. The characteristics and deformation of adjacent particles are affected more than those of distant particles in this approach, and the function corresponds to the shape function in the classic Lagrangian finite element method. SPH is primarily utilised in fluid dynamics modelling by establishing a free surface between two interacting fluids, and mass conservation is enforced to mimic fluid motion. By addressing instabilities, solution accuracy and lack of consistency in material deformation, the SPH approach is expanded to solid mechanics applications. During impact welding, the wavy morphology and jetting phenomena may be anticipated using SPH.

An axisymmetric SPH simulation is performed using ANSYS Autodyne (Fig. 5) to study the waviness formation during MPW of the D9 tube on the SS 316LN end plug. The flow chart of the process is shown in Fig. 1. Fig. 5 represents the required geometry for SPH modelling of the welding morphology at the interface. The model considers the D9 tube and SS 316LN end plug inclined at an angle as per the design before the initial contact/impact. The contact velocity of the D9 tube is calculated from the Lagrangian model and used as an input to the SPH simulation model. Particle size of 5 µm is decided for both materials during SPH to study the interfacial morphology and jetting. Both components are assumed to be 3 mm from the point of contact, that has been observed to be sufficient for waviness generation as per experimental results. Room temperature is fixed as the initial temperature, replicating the experimental conditions.

Furthermore, a constant value velocity is applied in the negative y-direction to the outer surface of the working zone. The only boundary condition is to fix the bottom edge of the end plug, constrain the left edge of the tube, and end plug vertically. The Johnson-Cook material model with the constants given in Table 1 is used to study the material deformation.

Preprint

Corresponding Author Email: kumar176103003@iitg.ac.in

5. Experimental setup

For welding of the D9 tube to the SS316LN end-plug, an indigenously designed electromagnetic machine with a maximum charging energy of 70 kJ at a voltage of 25 kV is employed, as has been discussed by Kumar et al. [40-41]. The electromagnetic processing system consists of two capacitor sub-banks, each with a single trigatron type switch. To close the switch simultaneously with minimal jitter, a specially developed trigger generator is used. These operational characteristics of capacitor banks are determined by trial and error. The maximum current and short circuit frequency are 700 kA and 22 kHz, respectively. The minimal work thickness to be welded is constrained by this frequency as the skin depth should be smaller than the job thickness, which is highly dependent on the current frequency. A four-disc bitter coil has been constructed for this experiment [41]. The principal function of the coil is to conduct current and provide an appropriate magnetic field and pressure distribution. A bitter type coil is insufficient to meet the required magnetic field because it loses mechanical integrity at such high magnetic fields and fails catastrophically before achieving the requisite magnetic field. Using a multi-turn coil with a fine winding pitch to raise local field intensity is also difficult due to the increased coil inductance. Therefore, a disposable copper field shaper is used for the process along with the bitter type coil, which contributes to the mechanical integrity of the coil and further distributes and intensifies the magnetic field in the working zone [42]. Fig. 6 demonstrates the electromagnetic manufacturing machine setup consisting of the bitter coil, a disposable field shaper and metallic fixtures to hold the workpiece axially.

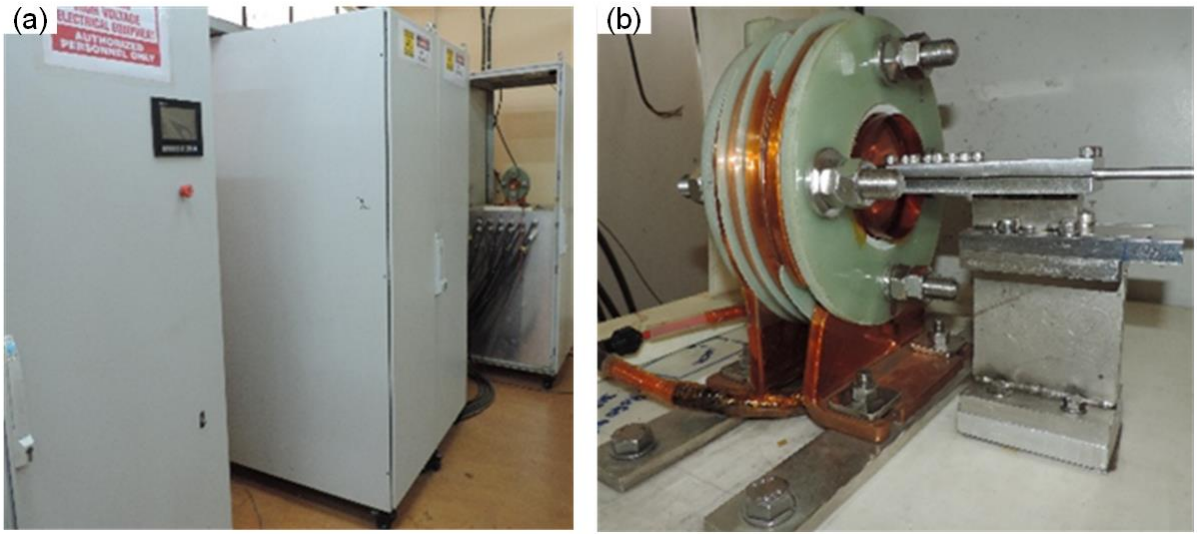

Fig. 6 Machine used: (a) 70kJ/25kV magnetic welding machine, (b) Welding tool consisting of Bitter coil with disposable copper field shaper and

The MPW generates an extremely strong magnetic field B_{max} of more than 40T and a rise time of less than 25 μs which results in a dynamic pressure of more than 640 MPa.

Corresponding Author Email: kumar176103003@iitg.ac.in

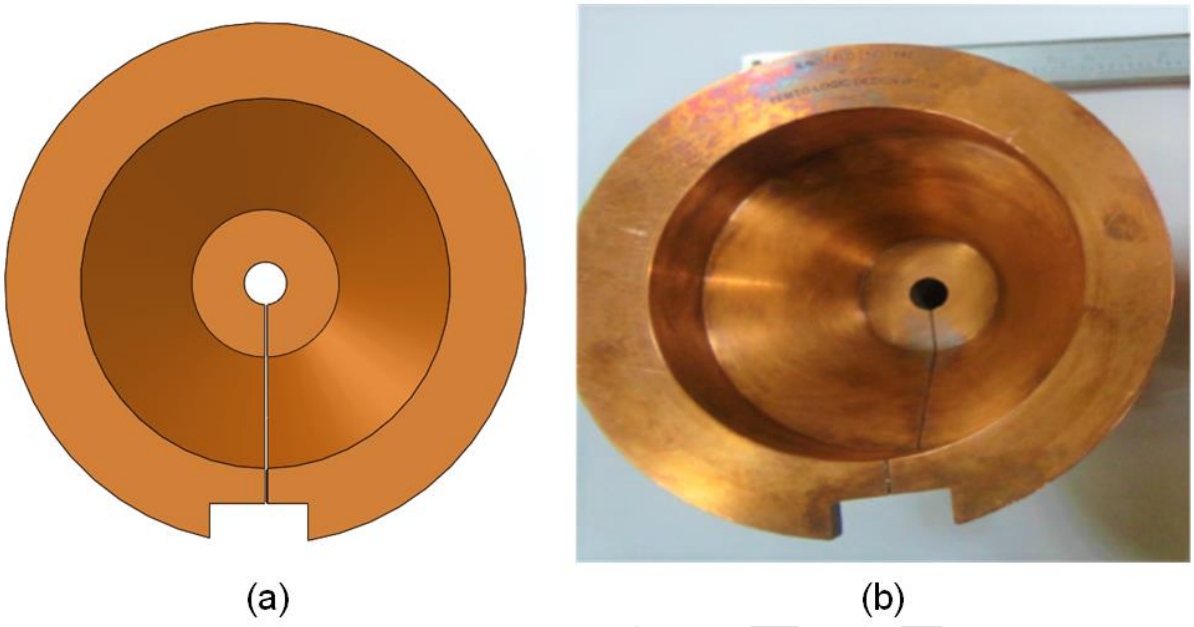

Fig. 7 Copper field shaper (a) top view, (b) experimental sample

The magnetic pressure exceeding the yield strength of the field shaper material leads to residual plastic deformation, accumulating in every successive pulse, causing the progression of deformation and further reducing field strength over the usage. Therefore, developing a mechanically robust field shaper with materials like Cu-Be, Cu-Ti, Cu-Cr-Zr, and Al-Sn alloys having relatively higher conductivity (greater than 15% IACS) is a necessity. However, these materials get to suffer from saw-effect at magnetic fields above 40 T (minimum required magnetic field for welding D9 steel tubes [43]) because of the melting of the field shaper material at sharp corners in the field shaper, caused by high eddy current density. Due to the saw-effect, the field shaper is not suitable for many shots, and the only option is to utilise disposable field shapers. Therefore, replaceable inserts made of Cu, Al, Nb, Ta, SS, C-W, and Ta are used with hybrid field shapers. However, arcing at the interface of the field shaper and the insert at the slit site affect these replaceable insert field shapers, making them unsuitable for use in an industrial machine as also discussed by Kulkarni et al. [44].

Furthermore, it has been observed that the slit in the field shaper leads to an asymmetrical force distribution on the clad tube in the working zone, as discussed by Kumar et al. [45], causing bending of the joint towards the slit side. This bending problem in the weld portion is mitigated by designing an innovative fixture as shown in Fig. 6 (b), which minimises the bending effect. This modification in the fixture has made all MP welded joints within acceptable dimensional tolerances. D9, which is used as a clad tube material, is a nuclear-grade austenitic stainless steel with broad applications in fuel pin cladding and other core components [1]. It has an operating temperature up to 923K. A tapered SS 316LN rod is used as an end plug. The chemical composition of D9 and SS 316LN is obtained using EDS (energy-dispersive X-ray spectroscopy) and compared with the standards as shown in Table 3. Here, as the D9 steel tube has poor electrical conductivity and high yield strength, the magnetic field induces a lower

Corresponding Author Email: kumar176103003@iitg.ac.in

eddy current resulting in very low effective pressure for welding even at a higher magnetic field (50T). A high electrically conductive copper tube called 'driver' is used as a sleeve around the tube to address this problem. This driver translates Lorentz's forces effectively on the tube to be welded, and its thickness is chosen equal to that of magnetic skin depth [1]. The driver tube gets damaged after each welding shot. The geometry of the driver and the clad tube is kept constant throughout the experiment. The taper design of the end plug ensures its self-cleansing during impact, and it also resists the resulting stress wave. The geometry of the end plug is considered as one of the most critical factors for achieving a successful weld. Therefore, the taper angle and tapered length of the end plug are optimised for the D9 steel tube by trial and error. All angles between 6° to 9° have resulted in a proper weld, but 8° has produced the longest welding joint of 5 mm. Due to the high pulsed forces, the driver and flyer accelerate towards the end plug and collide with a high velocity in the ranges of 300–500 m/s, resulting in a metallic bonding between the tube and the end plug. All trials are conducted in atmospheric conditions. Four discharge voltages are tried (15 kV, 16 kV, 17 kV and 18 kV). Process parameters are shown in Table 4. The stand-off distance between the tube and end plug increases gradually along the collision direction due to the taper angle, enabling it to attain an optimum collision velocity. The mechanical properties of the Cu and D9 tubes are shown in Table 5.

Table 3 Chemical composition of D9 tube and SS 316LN metallic plug

Element	C	Ni	Cr	Mo	Ti	Si	Mn	N	Fe
D9 tube	0.04	15.5	14.04	2.25	0.26	0.61	1.78	0.0037	Balance
SS316 LN	0.03	14	18	-	-	0.33	1.88	0.044	Balance

Table 4 Process parameters of the experiment

Discharge voltage (kV)	15	16	17	18
Current (kA)	310	334	354	374
Taper angle (degrees)	8°	8°	8°	8°

Table 5 Mechanical and electrical properties of driver and flyer material

Material	Yield strength (Mpa)	Ultimate tensile strength (MPa)	Elongation	Magnetic permeability	Electrical conductivity (MS/m)
Copper	70	210	60%	0.99	58.7
D9	550	770	20%	1.02	1.351

Preprint

Corresponding Author Email: kumar176103003@iitg.ac.in

6. Results and discussions

6.1. Lagrangian Finite element model

The deformation pattern of the D9 tube over the SS 316LN end plug shows effective plastic strain in the working zone of the magnetic pulse welding joint in the numerical simulation model (Fig. 4(b)) using ANSYS explicit dynamics at 18 kV of discharge voltage for four different time values is shown in Fig. 8. A convergence study is conducted for various mesh sizes. to ensure convergence with mesh refinement

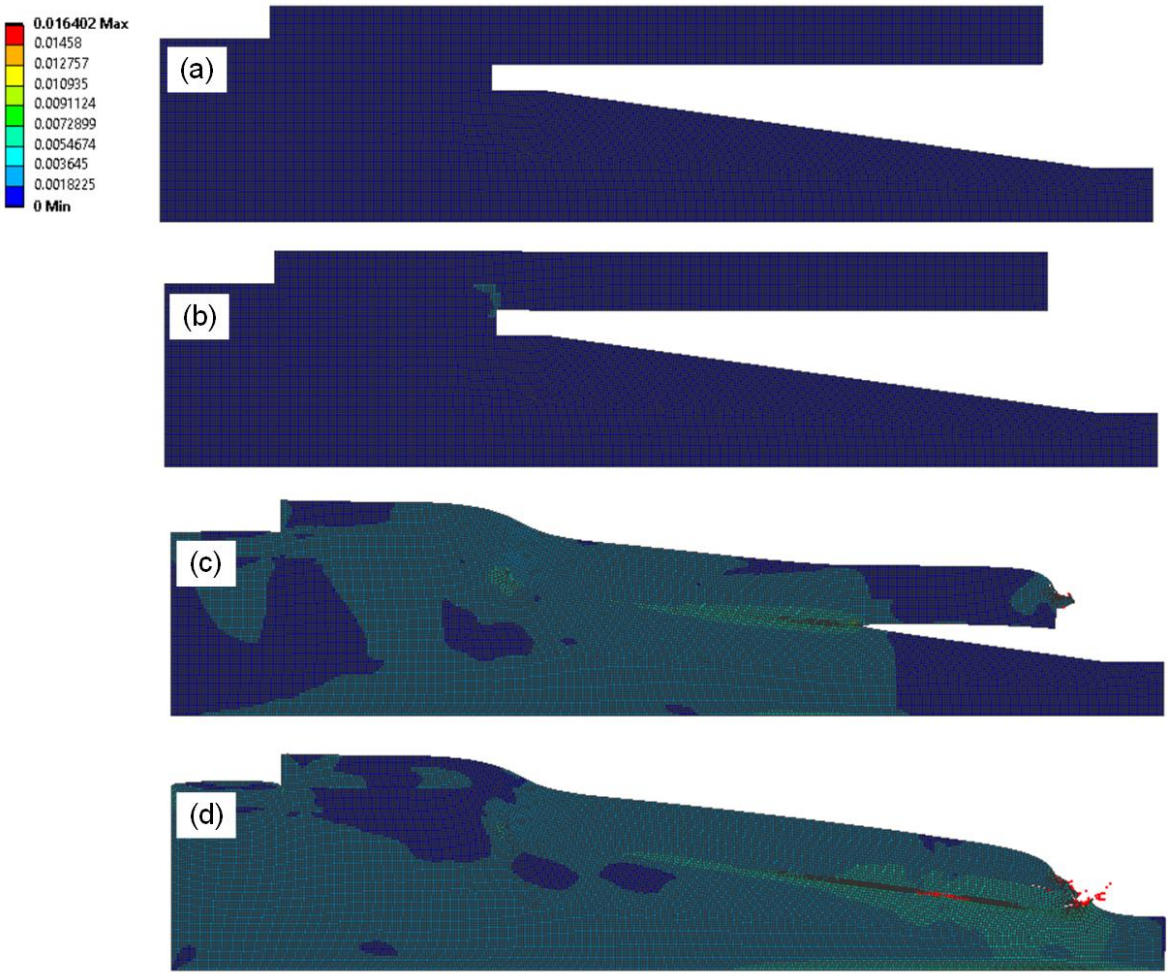

Fig. 8 Deformation stages showing the effective plastic strain fringe pattern of MPW joint at four different times (a) 0 µs, (b) 5 µs, (c) 10 µs and (d) 15 µs at 18 kV of discharge voltage

Corresponding Author Email: kumar176103003@iitg.ac.in

6.2. Experimental validation of Lagrangian simulation model

The outer diameter of the tube-to-end plug (D9-SS 316LN) joint is experimentally measured using an optical microscope of low magnification and compared with the results obtained from Lagrangian simulation. Fig. 9 shows the experimentally and numerically observed variations of the outer diameter (averaged circumferentially) of the D9 tube-SS 316LN tube-to-end plug assembly after welding at four different locations (2mm, 5 mm, 9 mm and 12 mm) along the axis in the working zone for two different discharge voltages (18 kV and 17 kV). Deformation increases with an increase in discharge voltage, and the minimum value of outer diameter is observed at 18 kV of discharge voltage. Experimentally calculated values align with the simulated results with a 2-5.1 % error. It is observed that the experimental values of the outer diameter in the working zone are lower than the simulated values, and this is probably due to the assumption that the current is uniformly distributed in the cross-section of the solenoid coil leading to an increase in deformation due to the increased Lorentz force.

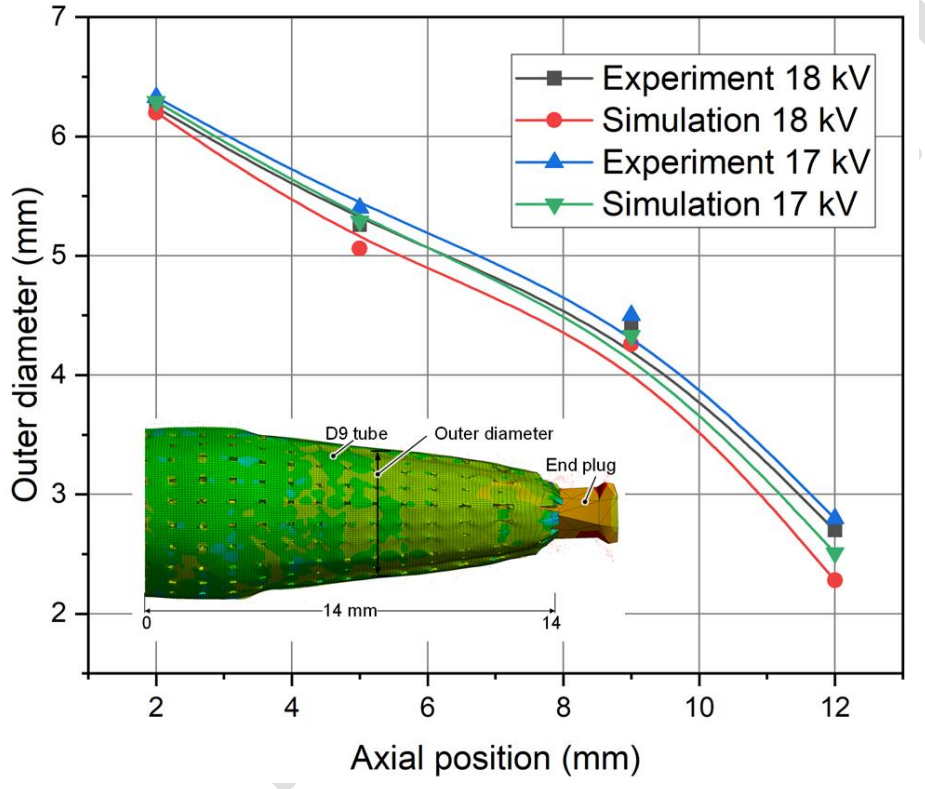

Fig. 9 Outer diameter comparison of the D9 tube-SS 316LN end plug joint in the working zone

6.3. SPH results along with experimental validation

As the particles in SPH are not connected, their relative movement facilitates to a model of metal jet emission, which mesh-based numerical approaches could not do. Jetting is thought to be a requirement for welding as it removes nascent oxides and impurities from the mating

Corresponding Author Email: kumar176103003@iitg.ac.in

surfaces, allowing solid-state bonding to occur without substantial melting or long-range diffusion. The SPH approach accurately recreated metal jet emission during impact welding. The interface morphologies of the joint at different time frame during simulation is shown in Fig. 10. The initial input radially inward velocity is 540 m/s, and the initial angle is 8 degrees. A metal jet is released from the collision location when the flyer tube collides with the target end-plug. The metal jet's velocity is estimated to be 1000–1200 m/s range. It is also discovered that the amount of expelled metal jet has increased with increasing impact velocity for a given collision angle. Fig. 11 shows the waviness as well as the jetting phenomenon. Fig. 11 illustrates that the jetting phenomena have removed around 10-15 μm layer (2-3 particles) from the surfaces of the D9 steel tube and SS 316LN end plug. The probable reason for same amount of surface material removal may be the same range of shear moduli of them. The ejected materials during the simulation account for the deposited particles outside the welded zone as observed in the experiments.

Preprint

Corresponding Author Email: kumar176103003@iitg.ac.in

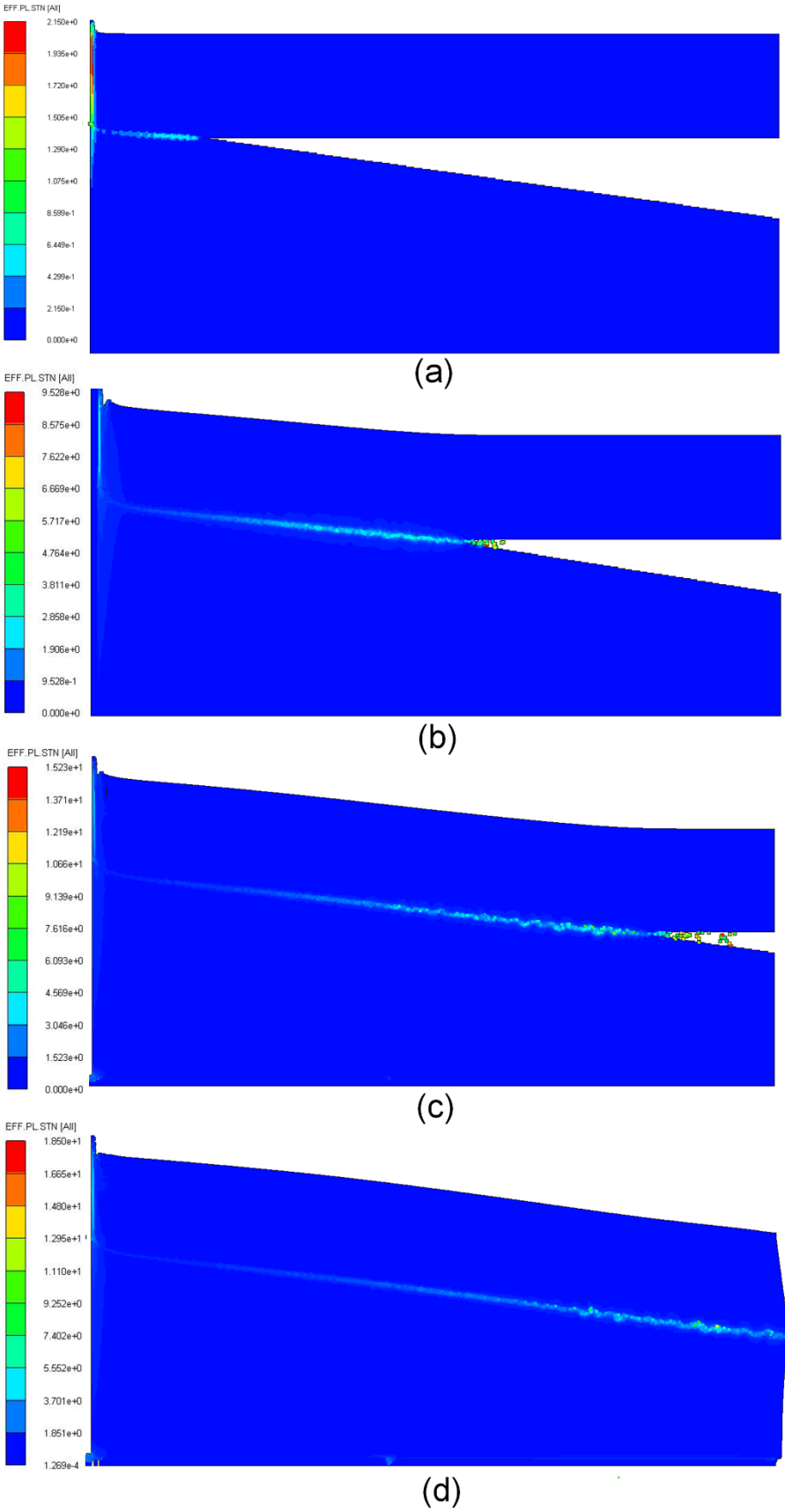

Corresponding Author Email: kumar176103003@iitg.ac.in

Fig. 10 SPH interface morphologies during simulation at (a) 0.12 μs, (b) 0.46 μs, (c) 0.64 μs and (d) 0.72 μs

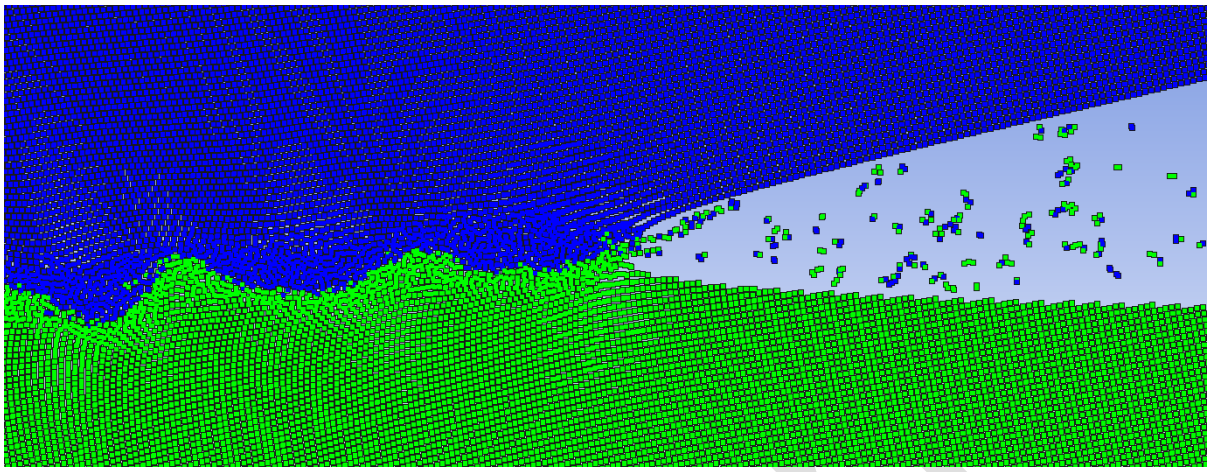

Fig. 11 Formation of wave structure and jetting during magnetic pulse welding simulation using SPH

Preprint

Corresponding Author Email: kumar176103003@iitg.ac.in

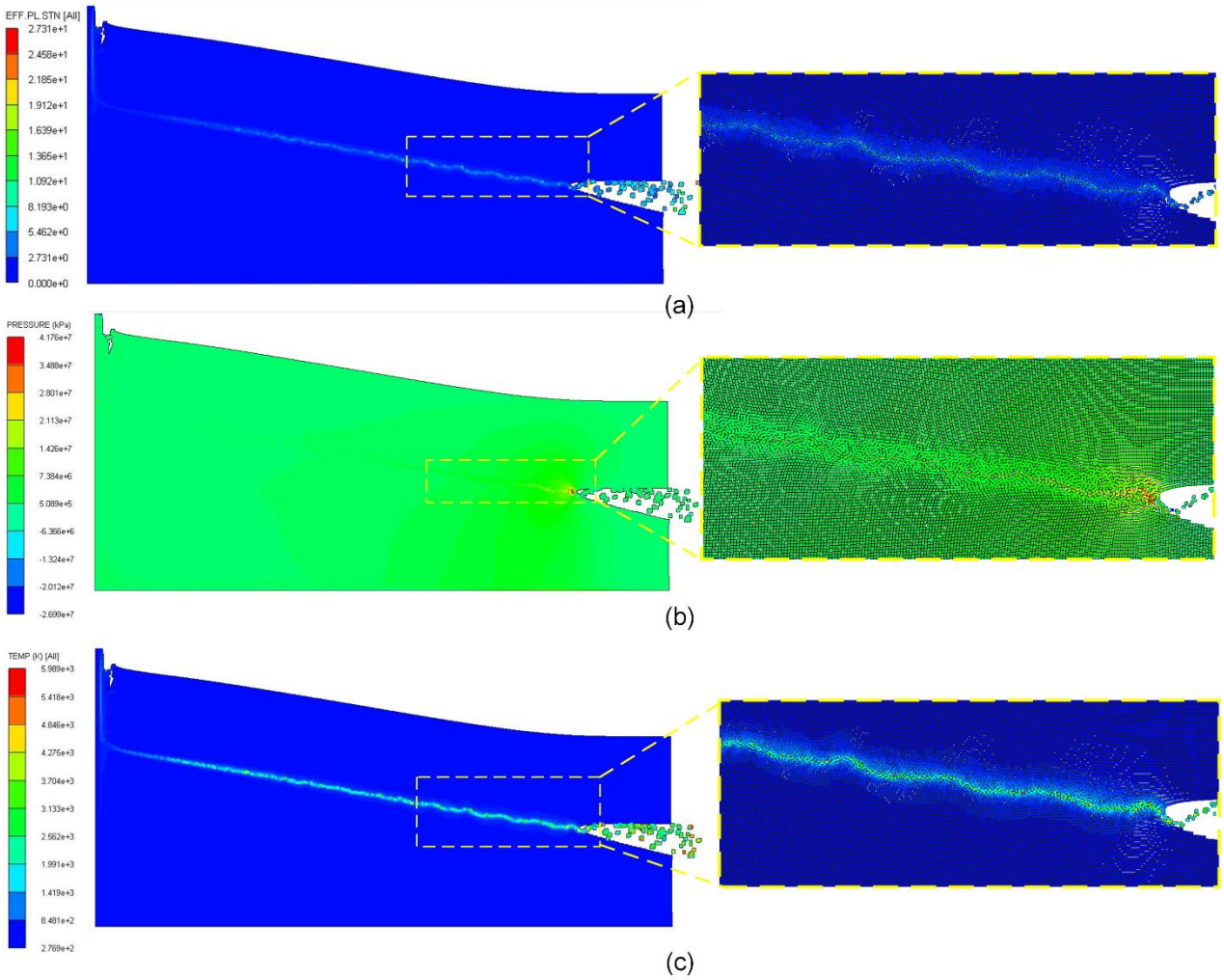

Fig.12 Predicted field variables at 1 µs for impact angle 8 degrees (a) effective plastic strain, (b) pressure and (c) temperature

Fig. 12 shows the field variables, effective plastic strain, pressure, and temperature after 1µs for the impact angle of 8 degrees. The effective plastic strain distribution (Fig. 12 (a)) shows high values, mainly in the range of 1 to 9, near the interface with a distance of 15-20 µm between both materials, while the rest of the workpieces remain elastic. Experiments show elongated grains at the interface, which are consistent with these high strain levels. Furthermore, such a common interfacial strain could be a source of kinematic instability. The pressure at the collision point is around 18 GPa, as shown in Fig. 12 (b). The anticipated temperature is strongly localised near the interface where significant plastic deformation develops, as seen in Fig. 12 (c). The thickness of this zone is around 30-55 µs. Predicting such a confined zone is critical since melting has long been thought to be undesirable for weld quality because of the intermetallic produced.

Corresponding Author Email: kumar176103003@iitg.ac.in

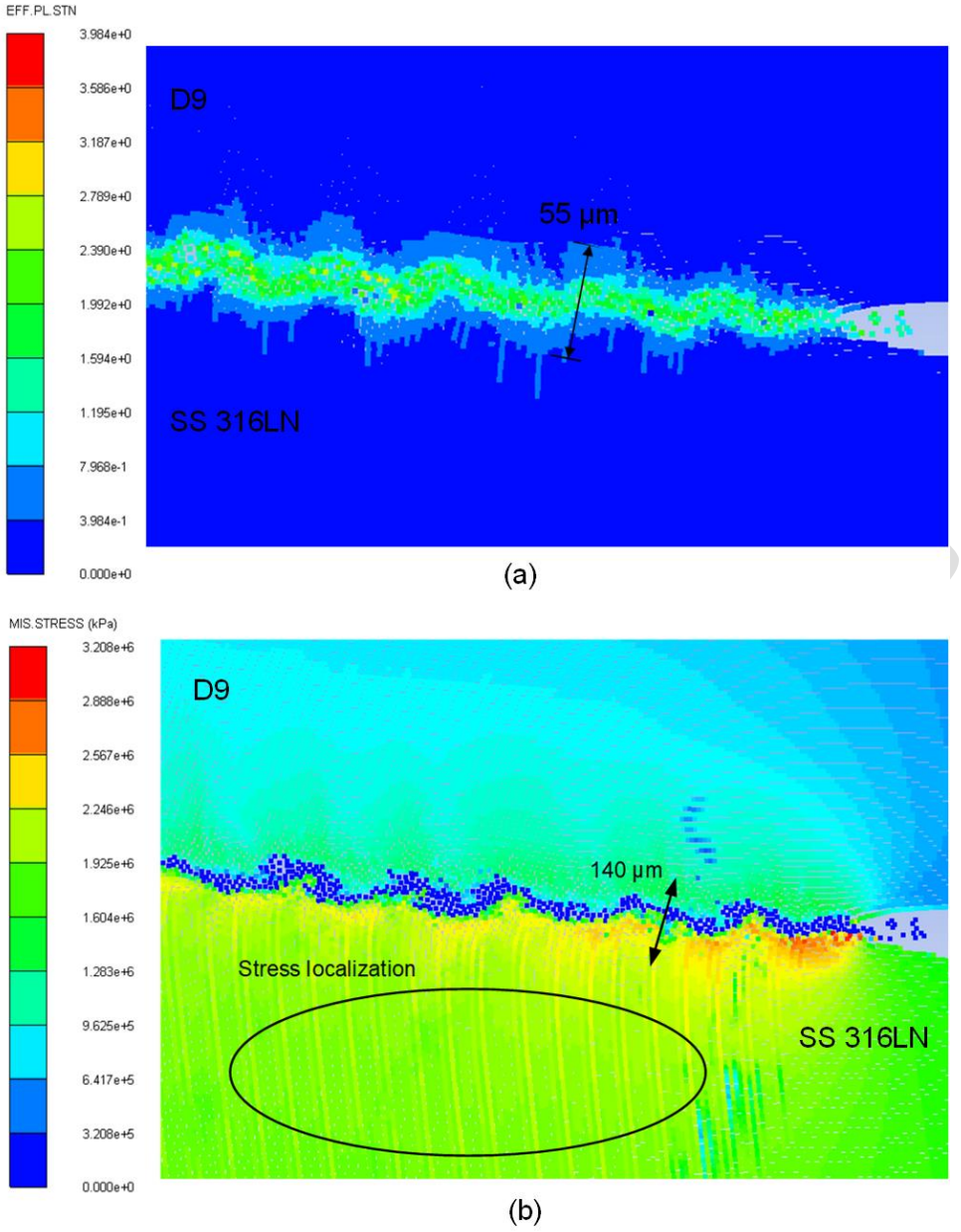

Fig. 13 Predicted (a) effective plastic strain and (b) von Mises stress fringe pattern at 3 µs for an impact velocity of 500 m/s and 8 impact angle of 8 degrees

Fig. 13 (a) further confirms localised plastic deformation in the immediate vicinity of the D9-SS 316LN interface in the range of 55 µm while the rest of the workpiece remains elastic. The significant strain value obtained near the interface aligns with the deformed/equiaxed grains obtained near the interface in experimental samples. Fig. 13 (b) shows the stress localisation in the SS 316LN side.

Corresponding Author Email: kumar176103003@iitg.ac.in

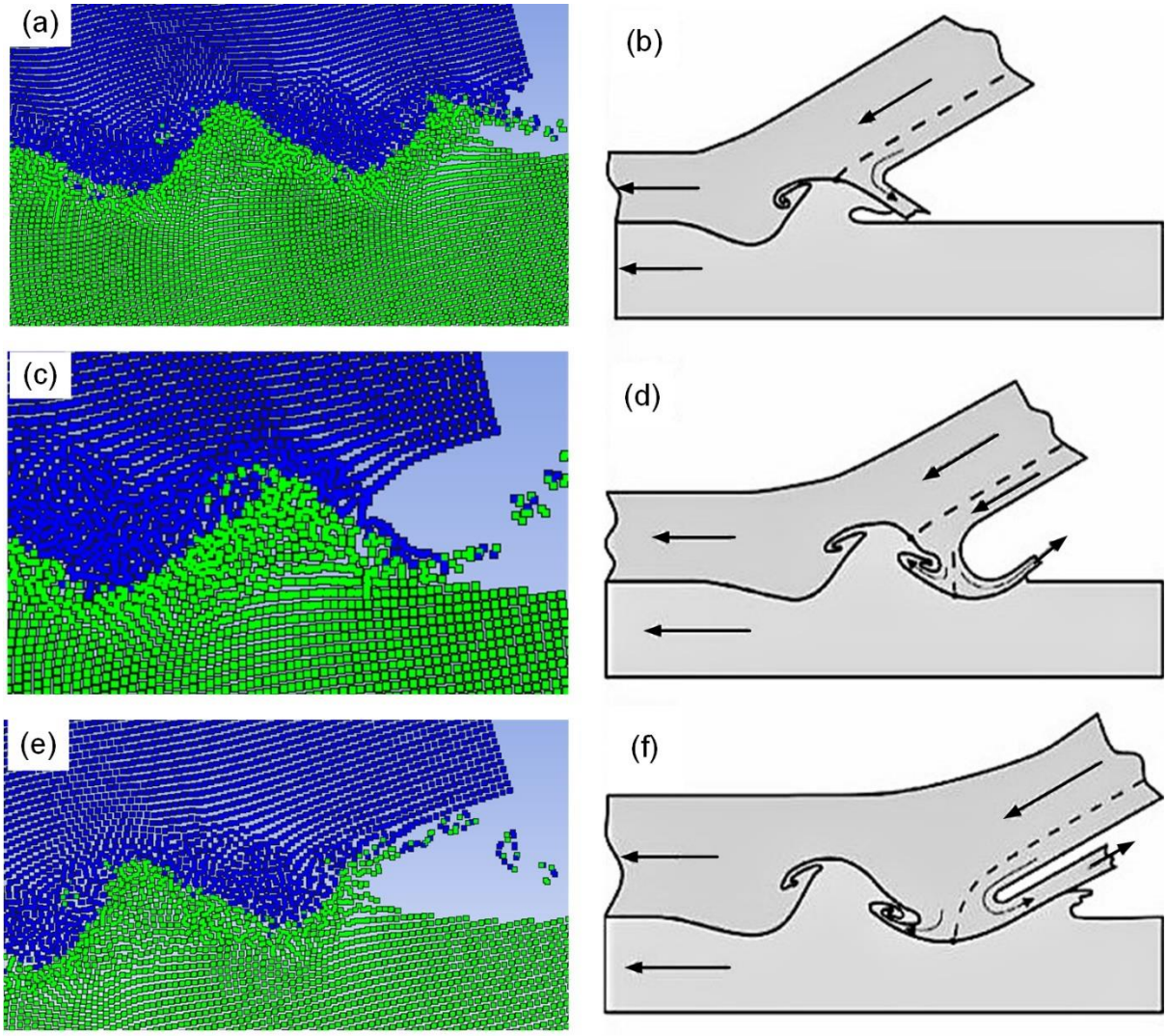

Fig. 14 Comparison of results of SPH simulation with the Bahrani-Black-Crossland wave formation model

One of the most exciting aspects of impact welding is the formation of waves at the interface. Many theoretical and practical research have been devoted for solving the problem in the early history of impact welding, one of which have been proposed by Abrahamson et al. [46], where the authors proposes indentation mechanism. The process of waviness formation has been further explored by Bahrani et al. [47], and it is now an often-cited explanations for the mechanics of wave propagation during impact welding. Furthermore, Hunt et al. [48], Cowan et al. [49], Robinson et al. [50], have attempted to characterise the wave generation during impact welding qualitatively and quantitatively. Hay et al. [51] discusses that the material behaves like a fluid under specific types of impact. The authors have used the hydrodynamic methodology to explain the material behaviour during high-velocity impact and in further elaborating the wave generation theory. However, Hay et al. remarked that a thorough explanation of the wave creation process using conventional hydrodynamic methodologies is difficult because of unavailability of vortex formation models for all Reynolds values [51]. Calculating metal viscosity over the range of strain rates is also challenging. According to the

Corresponding Author Email: kumar176103003@iitg.ac.in

data reported in the preceding sections, SPH simulation accurately reproduces the empirically obtained interface morphology (Fig. (14)) which More attention must be devoted to the movement of individual particles in the model to understand better the dynamics behind the generation of waves and vortex zones. Fig. 14 depicts a typical collision that results in the production of waves.

The collision point, which moves from left to right, is connected to the model's reference system, which follows the material flow of D9 steel flyer tube. In the Bahrani-Black-Crossland model, the flyer tube material is divided into two jets, one (salient jet) flows towards left and the other (re-entrant jet) towards right. The jet from the flyer tube interacts with one previous protrusion on the target tube in Fig. 14 (a). The jet is diverted downwards, deforming the target tube and forming a depression there (Fig. 14 (c, e)), and, as a result, a new protrusion rapidly grows at the tube contact just at the right of the depression (Fig. 14 (e)). This protrusion creates some depression on the flyer tube and further diverts the material flow of the flyer tube, as shown in Fig. 14 (a). These successive generations of depression and protrusions on both the flyer and the target tube materials create a wavy interface in the MP welded joint. Fig. 15 and Fig. 16 compare waviness morphology obtained at 18 kV of discharge voltage during SPH simulation as well as experiment. A good agreement in simulation and experimental result is obtained with the values of amplitude and wavelength of interface waviness being in close proximity.

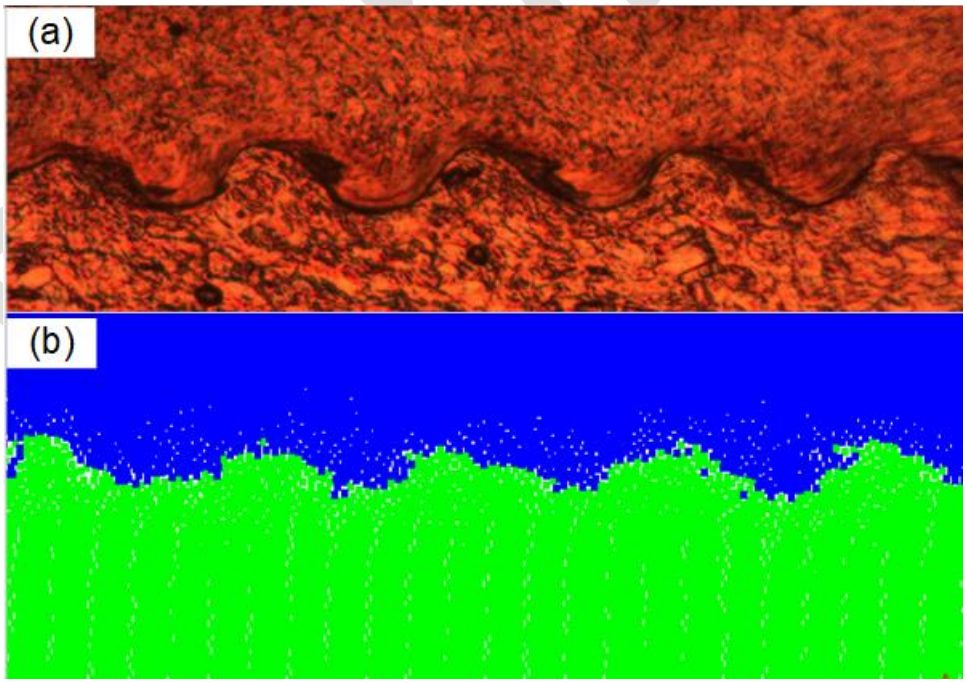

Fig. 15 Comparison of waviness morphology in (a) Experiments and (b) Simulation

Corresponding Author Email: kumar176103003@iitg.ac.in

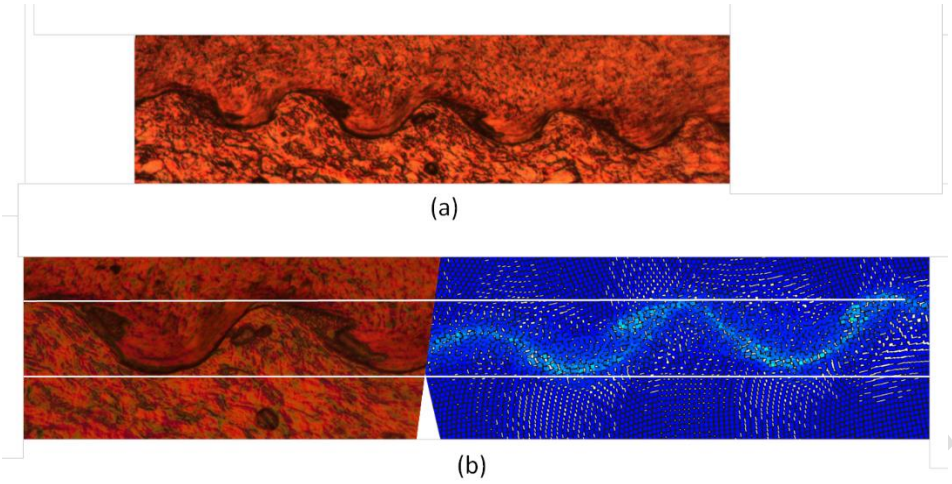

Fig. 16 (a) Optical micrograph showcasing waviness pattern of the welded interface in experiments (b) Comparison with SPH (zoomed view) at 8-degree, 18 kV discharge voltage

6.4. Hydraulic burst test

The strength of the tube-to-end plug junction has been analysed using a hydraulic pressure burst test at 300K. With the use of fluid, pressure is applied in all directions in this procedure. It is a destructive testing approach for estimating a part's pressure overload capability in pressurised settings [52]. To connect the joint to a hydraulic burst tester at one end, MPW samples are welded to a fixture tube (used to close the tube to end plug joint) using inert tungsten gas (TIG) welding. At 300 K, three samples are subjected to a hydraulic burst test. At pressures reaching 105 MPa, all three samples rupture near 108 MPa (Fig 17 (a)) at the D9 steel tube near the TIG welded joint region between D9 steel clad and the fixture tube (used to close the tube-to-end plug joint). This means that MPW joints are more durable than the weakest parent metals. Based on the first principle of the thin cylinder, this measured rupture pressure reasonably fits the tube's rupture strength.

Preprint

Corresponding Author Email: kumar176103003@iitg.ac.in

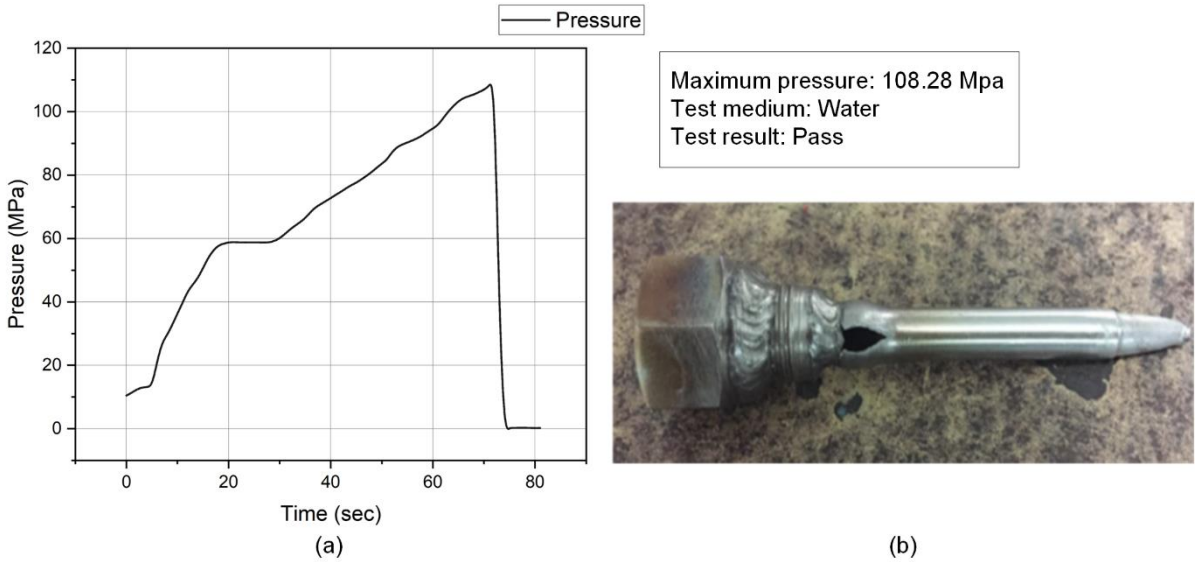

Fig. 17 (a) Pressure profile with time obtained from hydraulic burst test indicating the failure of the tube at 108 MPa and (b) Hydraulic burst sample failed at D9 tube near the TIG joint

6.5. Micro-hardness test

The hardness variation across the joint interface is measured using a micro-hardness tester with a 250 gm load. As illustrated in Fig. 18, the average microhardness values on the D9 side and the SS 316LN side are 309 VHN and 280 VHN, respectively. A 3-5 percent increase in hardness is noted on both sides of the contact, which can be attributed to the strain hardening during the MPW process.

Preprint

Corresponding Author Email: kumar176103003@iitg.ac.in

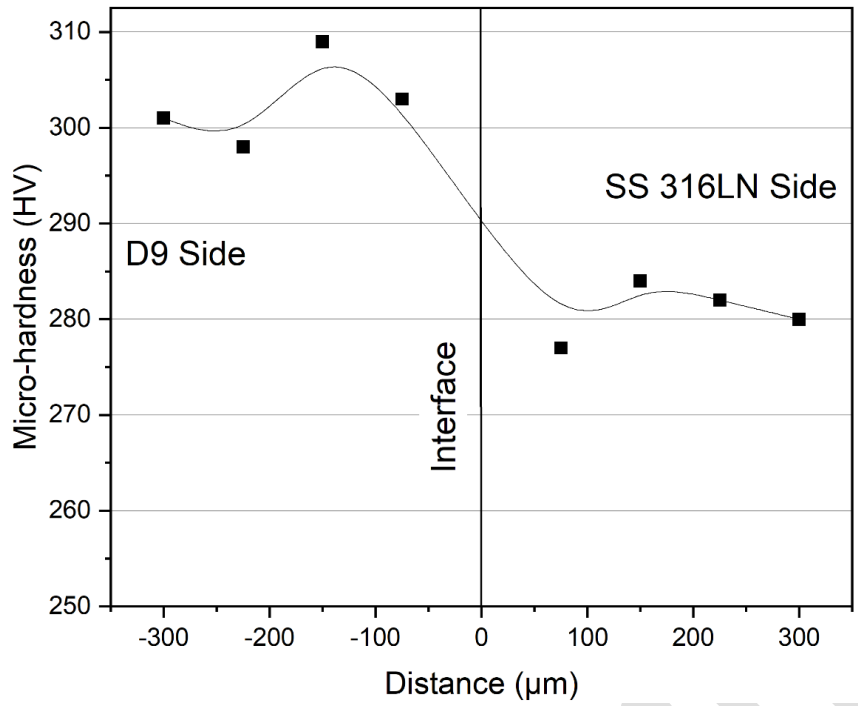

Fig. 18 Micro-hardness distribution near the bonding interface for the MP welded sample

6.6. X-ray computer tomography

X-ray computer tomography is a non-destructive technology for visualising several forms of three-dimensional data about a solid object, such as microstructure, flaws, and crystallography. Fig. 19 shows an X-ray tomography image of a D9-SS 316LN tube-to-end plug MP welded sample, demonstrating deformation of the D9 outer tube onto the tapered SS 316 LN end plug. The tomography used X-ray clearly distinguishes between a uniform welded region without any fracture and a non-uniform, irregular non-welded region with a gap along with the interface. The welding length is more than 5 mm from this tomography image. Fig. 20 shows the reconstructed voxel image of size 4 μm, which further confirms the non-uniformity at the D9-SS 316 LN interface at the beginning of the working zone. However, uniformity can be seen in the latter half of the working length as the welding proceeds in the welding direction. `

Corresponding Author Email: kumar176103003@iitg.ac.in

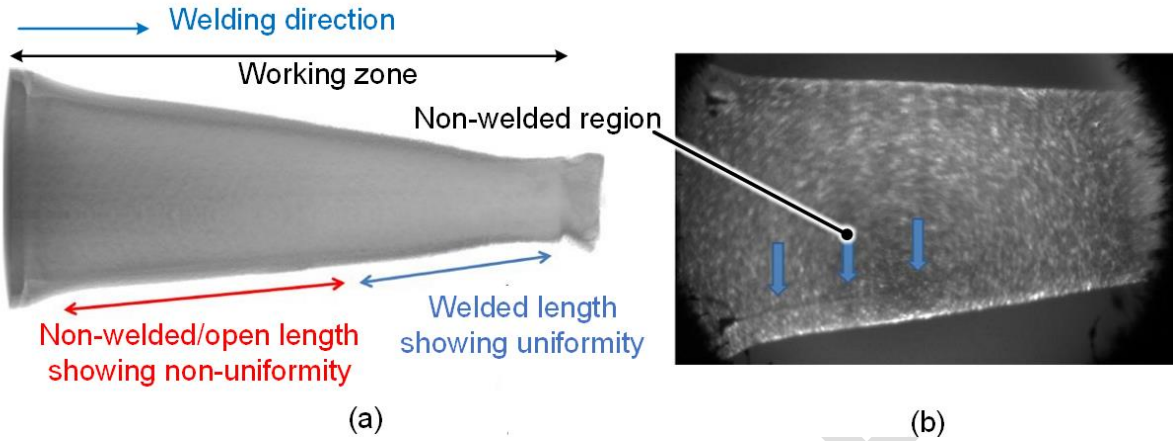

Fig. 19 (a) X-ray tomography of one of the samples and (b) high-resolution optical image indicating uniformity in the welded region

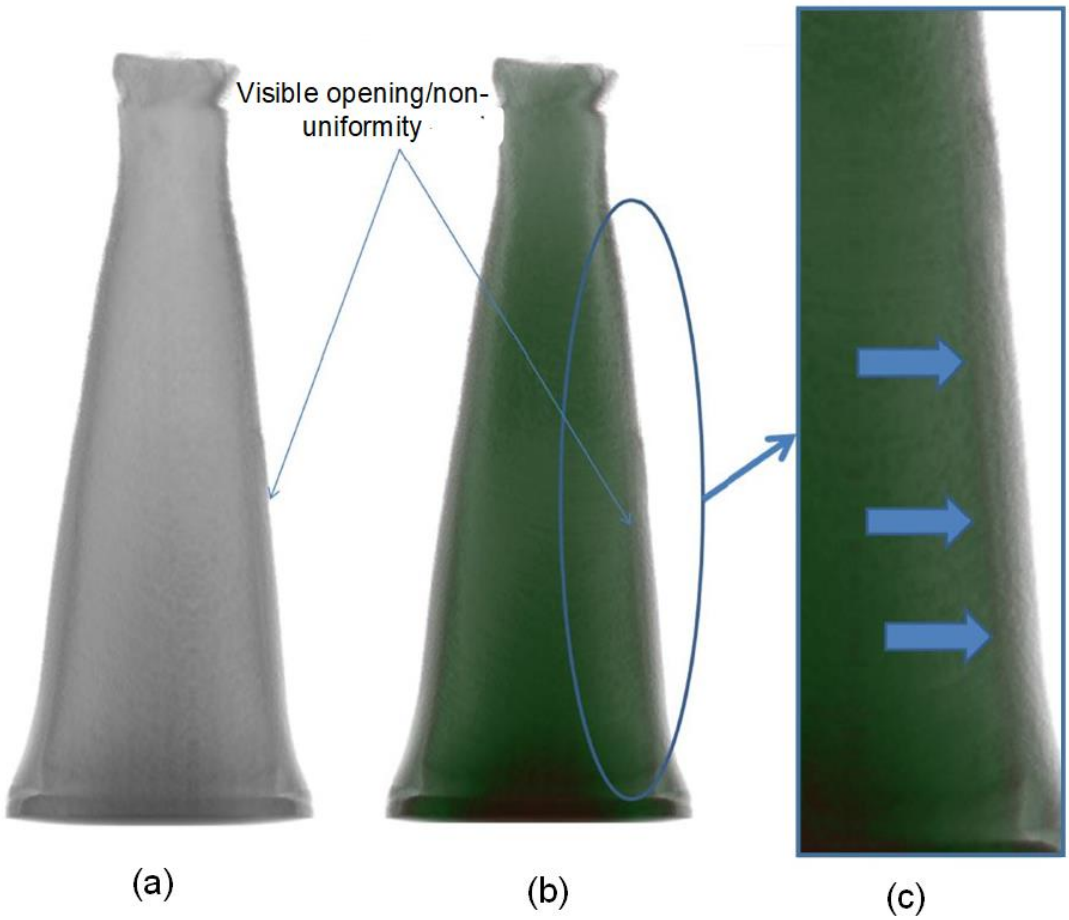

Fig. 20 (a) Half-cut sample micro-tomography, (b) reconstructed voxel (volume pixel) of the sample and (c) zoomed view showing opening/non-uniformity in welding at the D9-SS 316LN interface

Corresponding Author Email: kumar176103003@iitg.ac.in

6.7. Optical micrography and Scanning electron microscopy

The integrity of the MPW samples are checked in transverse and longitudinal directions using optical micrography (OM) and scanning electron microscopy. Samples are cut longitudinally and transversely using a WEDM (wire-cut electric discharge) machine to characterise the joint. During the cutting operation, adequate coolant is utilised to avoid any microstructural alterations. After that, silicon carbide (SiC) sheets having grit size in the range of 100-2000 in increasing order are used to ground the samples, followed by abrasive polishing. Fig. 21 show two optical micrographs of the D9-SS316 interface at 200 and 500 nm. Weld interface shows wavy morphology. These waviness patterns are caused by the jet from the flyer tube penetrating the target end plug surface at the point of impact. During high-velocity impact, Plastic deformation converts the grains to become semisolid near the interface leading to the hydrodynamic behaviour of metal [16]. Periodic and symmetric waves, comparable to explosive [54] and electromagnetic welding [55], have been shown in wavy morphologies, indicating good joint quality. The unwielded area shows no effect in grain morphologies. However, grains at the interface are severely distorted, mirroring the waviness phenomenon of the weld. Due to fluctuations in the magnetic field, the amplitude and wavelength of the waves alter gradually from the vertical centreline along with the interface MPW of sheets [16]. However, in this tube-to-end plug joining, the field shaper in the working zone produces a uniform magnetic field circumferentially, resulting in a series of homogenous waves with comparable amplitude and wavelength at the weld interface. The wavelength and amplitude are 32 and 73 metres, respectively. The intimate contact area and interlocks between two metal surfaces are increased by these wavy morphologies [16]. The deformation of the D9 tube causes grain refinement at the contact on the D9 side. The interface area is depicted in SEM pictures at various magnifications in Fig. 22. Kulkarni et al. [44] have conducted an EDS analysis of the experimental work to determine the composition at the interface area, which they discovered to be a combination of both metals.

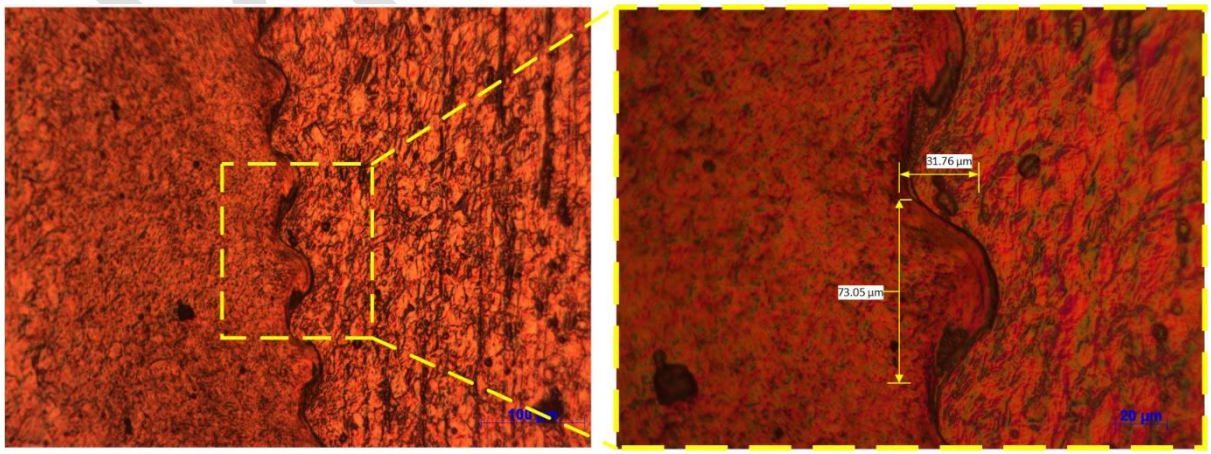

(a) (b)

Corresponding Author Email: kumar176103003@iitg.ac.in

Fig. 21 Optical micrographs at (a) 200× and (b) zoomed view at 500× showcasing the waviness pattern at the interface

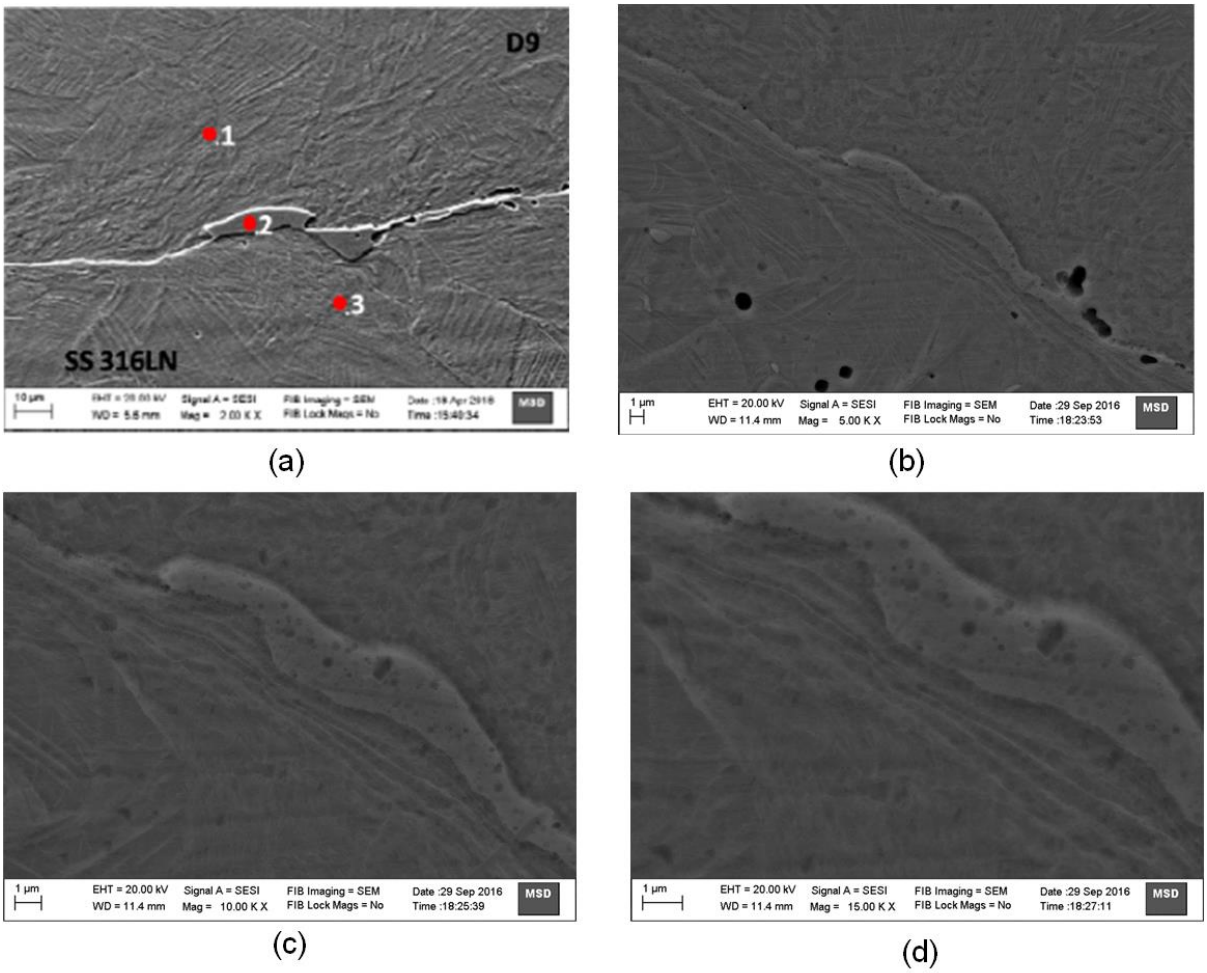

Fig. 22 SEM micrographs of the interface between SS 316LN and D9 at (a) 2.0K ×, (b) 5.0 K ×, (c) 10 K × and (d) 15.0 K ×

7. Conclusions

Magnetic pulse welding is used in this research to build a D9-SS 316LN tube-to-end plug junction. High-speed, flexible, and high-integrity weld joints are produced using a green and solid-state welding technique. The high-speed impact welding technique is being studied experimentally and simulated. Experimental procedures resulted in a leak-tight junction with wavy interface morphology and no defects. SPH simulation has recreated the same phenomenon. It is possible to draw the following conclusions.

- The Lagrangian mesh-based simulation indicates a good agreement of deformation with experimental results.

Corresponding Author Email: kumar176103003@iitg.ac.in

- The D9-SS316LN tube-to-end plug interface shows wavy morphology with narrow grain boundary-like bonding interfaces.
- The metal jet emission and weld interface morphology is reproduced successfully using the SPH method.
- The SPH simulation results are validated with the Bahrani-Black-Crossland wave formation mechanism.
- Hydraulic burst tests show failure in the base tube area near the TIG joint and not the MPW area, showcasing the excellent quality of the MPW joint.
- Samples show uniformity in the welded region in the working zone during X-ray tomography.
- OM and SEM analysis have been used to explore further the waviness morphology obtained in the SPH simulation.

Acknowledgements

The authors acknowledge the contribution made by Mrs. Supriya Barje for the timely preparation of required engineering drawings. The authors also like to thank the technical assistance rendered by Mr. Rajesh Kakad for conducting the experiments, Dr. R. Suresh Kumar, Head HTAS/SMD, IGCAR for conducting high pressure-temperature test. Mr.R. K. Rajawat, Head APPD & AD, BTDG, BARC and Dr. R. Tewari, Head MSD, BARC for the encouragement received during the development of this process. BRNS for financial support for this research work. Dr. Arup Nandy and Mr. Deepak kumar gratefully acknowledge the support from SERB, DST under the project IMP/2019/000276, and VSSC, ISROthrough MoU No.: ISRO:2020:MOU:NO: 480.

References

1. Mannan S L, Chetal S C, Raj B, Bhoje S B, Trans Ind Inst Met 52.6 (2003) 89.
2. Babkin L T, albertov K K, Sannikov D V, Yashunskii A Y, Peslyak O K, Weld Int 14 (2000) 162.
3. Harinath Y V, Gopal K A, Murugan S, Albert S K, J Nucl Mater 435 (2013) 32. https://doi.org/10.1016/j.jnucmat.2012.12.023.
4. Murugan A, Sai S R, Raju R, Lakshminarayanan A K, Albert S K, Adv Electron Forum 24 (2017) 40. https://doi.org/10.4028/www.scientific.net/aef.24.40

5. Cui, J.; Sun, G.; Li, G.; Xu, Z.; Chu, P.K. Specific wave interface and its formation during magnetic pulse welding. Appl. Phys. Lett. 2014, 105, 221901.

Preprint

Corresponding Author Email: kumar176103003@iitg.ac.in

6. Shankar, V., Gill, T.P.S., Mannan, S.L. et al. Solidification cracking in austenitic stainless steel welds. Sadhana 28, 359–382 (2003) https://doi.org/10.1007/BF02706438
7. chard E.: Welding metallurgy of stainless steels, Springer Verlag, New York, 1998.
8. Brooks J.A. and Thompson A.W.: Microstructural development and solidification cracking susceptibility of austenitic stainless-steel welds, International Materials Reviews, 1991, vol. 36, no. 1, pp. 16-44.
9. Srinivasan, G., Divya, M., Albert, S.K. et al. Study of Hot Cracking Behaviour of Nitrogen-Enhanced Austenitic Stainless Steels using Varestraint and Hot Ductility Tests. Weld World 54, R322–R332 (2010). https://doi.org/10.1007/BF03266746
10. S. Noh, R. Kasada, N. Oono, N. Iwata, and A. Kimura: Fusion Eng. Des., 2010, vol. 85, pp. 1033–37
11. Patra, S., Arora, K., Shome, M., and Bysakh, S., 2017, "Interface Characteristics and Performance of Magnetic Pulse Welded Copper-Steel Tubes," J. Mater. Process. Technol., 245, pp. 278–286. https://doi.org/10.1016/j.jmatprotec.2017.03.001
12. Raoelisona RN, Sapanathan T, Buiron N, Rachik M (2015) Magnetic pulse welding of Al/Al and Al/Cu metal pairs: consequences of the dissimilar combination on the interfacial behaviour during the welding process. J Manuf Process 20:112–127. https://doi.org/10.1016/j.jmapro.2015.09.003
13. Haiping Yu, Zhisong Fan, Chunfeng Li, Magnetic pulse cladding of aluminum alloy on mild steel tube, Journal of Materials Processing Technology, Volume 214, Issue 2, 2014, Pages 141-150, ISSN 0924-0136, https://doi.org/10.1016/j.jmatprotec.2013.08.013.
14. R. Shotri, K. Faes, A. De, Magnetic pulse welding of copper to steel tubes–Experimental investigation and process modelling, Journal of Manufacturing Processes, Volume 58, 2020, Pages 249-258, https://doi.org/10.1016/j.jmapro.2020.07.061.
15. Psyk, V., Risch, D., Kinsey, B., Tekkaya, A., and Kleiner, M., 2011, "Electromagnetic Forming—A Review," J. Mater. Process. Technol., 211(5), pp. 787–829.
16. Kapil, A., and Sharma, A., 2015, "Magnetic Pulse Welding: An Efficient and Environmentally Friendly Multi-Material Joining Technique," J. Cleaner Prod., 100(1), pp. 35–58.
17. Faes, K.; Kwee, I.; De Waele, W. Electromagnetic Pulse Welding of Tubular Products: Influence of Process Parameters and Workpiece Geometry on the Joint Characteristics and Investigation of Suitable Support Systems for the Target Tube. Metals 2019, 9, 514.
18. Junjia Cui, Guangyong Sun, Junrui Xu, Zhidan Xu, Xiaodong Huang, Guangyao Li,A study on the critical wall thickness of the inner tube for magnetic pulse welding of tubular Al–Fe parts, Journal of Materials Processing Technology, Volume 227, 2016, Pages 138-146, ISSN 0924-0136, https://doi.org/10.1016/j.jmatprotec.2015.08.008.
19. Shobhna Mishra, Surender Kumar Sharma, Satendra Kumar, Karuna Sagar, Manraj Meena, Anurag Shyam, 40kJ magnetic pulse welding system for expansion welding of aluminium 6061 tube, Journal of Materials Processing Technology, Volume 240, 2017, Pages 168-175, ISSN 0924-0136, https://doi.org/10.1016/j.jmatprotec.2016.09.020.
20. J. Lueg-Althoff, J. Bellmann, M. Hahn, S. Schulze, S. Gies, A.E. Tekkaya, E. Beyer, Joining dissimilar thin-walled tubes by Magnetic Pulse Welding, Journal of Materials

Preprint

Corresponding Author Email: kumar176103003@iitg.ac.in

Processing Technology, Volume 279, 2020, 116562, ISSN 0924-0136, https://doi.org/10.1016/j.jmatprotec.2019.116562.

21. Shotri R, Faes K, Racineux G, De A. Analytical Estimation of Electromagnetic Pressure, Flyer Impact Velocity, and Welded Joint Length in Magnetic Pulse Welding. *Metals*. 2022; 12(2):276. https://doi.org/10.3390/met12020276
22. Lee, JG., Park, JJ., Lee, MK. et al. End Closure Joining of Ferritic-Martensitic and Oxide-Dispersion Strengthened Steel Cladding Tubes by Magnetic Pulse Welding. Metall Mater Trans A **46,** 3132–3139 (2015). https://doi.org/10.1007/s11661-015-2905-5
23. Vivek A, Liu B, Hansen S, Daehn GS (2014) Accessing Collision Welding Process Window for Titanium/Copper Welds with Vaporizing Foil Actuators andnGrooved Targets. Journal of Materials Processing Technology 214(8):1583–1589.
24. Blazynski TZ (1983) Explosive Welding, Forming and Compaction, Springer.
25. Godunov SK, Deribas AA, Zabrodin AV, Kozin NS (1970) Hydrodynamic Effects in Colliding Solids. Journal of Computational Physics 5(3):517–539.
26. Lee T, Zhang S, Vivek A, Kinsey B, Daehn G (2018) Flyer Thickness Effect in the Impact Welding of Aluminium to Steel. Journal of Manufacturing Science and Engineering 140(12):1–7.
27. Jaramillov D, Inal OT, Szecket A (1987) Effect of Base Plate Thickness on Wave Size and Wave Morphology in Explosively Welded Couples. Journal of Materials Science 22(9):3143–3147.
28. Ben-Artzy A, Stern A, Frage N, Shribman V, Sadot O (2010) Wave Formation Mechanism in Magnetic Pulse Welding. International Journal of Impact Engineering 37(4):397–404.
29. S. Kakizaki, M. Watanabe and S. Kumai: J. JILM 61 (2011) 328333
30. Jiedi Li, Shinji Muraishi, Shinji Kumai, Experimental and Numerical Analyses of Wavy Interface Formation and Local Melting Phenomena at the Magnetic Pulse Welded Al/Fe Joint Interface, MATERIALS TRANSACTIONS, 2021, Volume 62, Issue 8, Pages 1184-1193, July 25, 2021, https://doi.org/10.2320/matertrans.LM2021828
31. M. Sarvari, A. Abdollah-Zadeh, H. Naffakh-Moosavy, A. Rahimi, H. Parsaeyan, "Investigation of collision surfaces and weld interface in magnetic pulse welding of dissimilar Al/Cu sheets," J Manuf. Process., pp. 356-367, Sep. 2019.
32. H. Yu, H. Dang, Y. Qiu,. "Interfacial microstructure of stainless steel/aluminum alloy tube lap joints fabricated via magnetic pulse welding," J Mater. Process. Technol., 2017.
33. A. Stern, O. Becher, M. Nahmany, D. Ashkenazi, V. Shribman. "Jet Composition in Magnetic Pulse Welding: Al–Al and Al-Mg Couples," Welding Journal, 2015, 94(8):258s–264s.
34. Faes, K.; Shotri, R.; De, A. Probing Magnetic Pulse Welding of Thin-Walled Tubes. J. Manuf. Mater. Process. 2020, 4, 118. https://doi.org/10.3390/jmmp4040118
35. Kwee, I. Faes, K. Interfacial Morphology and Mechanical Properties of Aluminium to Copper Sheet Joints by Electromagnetic Pulse Welding. Key Eng. Mater. 2016, 710, pp. 109–114.

Preprint

Corresponding Author Email: kumar176103003@iitg.ac.in

36. Kumar, D., Kore, S. D., and Nandy, A. (October 27, 2020). "Finite Element Modeling of Electromagnetic Crimping of Cu-SS Tube-to-Tube Joint Along With Simulation of Destructive Testing for Strength Prediction of the Joint." ASME. J. Manuf. Sci. Eng. April 2021; 143(4): 041004. https://doi.org/10.1115/1.4048431
37. Nikolaos E. Karkalos, Angelos P. Markopoulos, Determination of Johnson-Cook material model parameters by an optimisation approach using the fireworks algorithm, Procedia Manufacturing, Volume 22, 2018, Pages 107-113, ISSN 2351-9789, https://doi.org/10.1016/j.promfg.2018.03.017.
38. Do Young Kim, Dong Min Kim, OBum Kwon, Hyung Wook Park, Simulation of the round insert face milling process of AISI 316LN stainless steel with machining-based plastic behavior modelling, Proc IMechE Part B: J Engineering Manufacture 2021, Vol. 235(3) 443–454, DOI: 10.1177/0954405420958845.
39. Maria, C., 2009, Technology of EHIS (Stamping) Applied to Production of Automotive Parts. Saint-Petersburg State Polytechnical University, Department of Applied Mathematics
40. Kumar, S., Dey, G.K., & Sharma, A. (2019). An Investigation on Weldability of Flared D9 Tube to Cylindrical SS316L (N) Plug Using Electro-Magnetic Compression Welding. Open Access Library Journal, Vol.6 No.5, 2019 DOI: 10.4236/oalib.1105465
41. Kumar, S., Dey, G.K. and Sharma, A. (2020) Optimisation of Process Parameters in Electromagnetic Welding of D9 Tube to SS316 L (N) Plug. Open Access Library Journal, 7: e6346. https://doi.org/10.4236/oalib.1106346
42. Kumar D, Kore SD, Nandy A. Interference-fit joining of Cu-SS composite tubes by electromagnetic crimping for different surface profiles. Weld World 2021. https:// doi.org/10.1007/s40194-021-01081-8
43. Furth,H.P., Levinne,M.A. and Waniek,R.W., "Production and Use of High Transient Magnetic Field-II, Review of Scientific Instruments 28(11):7768-7770, 1979
44. Kulkarni, M.R., Kolge, T., Kumar, D. et al. Magnetic Pulse Welding of D9 Steel Tube to SS316LN End Plug. Trans Indian Inst Met **75,** 171–182 (2022). https://doi.org/10.1007/s12666-021-02413-4
45. Deepak Kumar, Sachin D. Kore, Arup Nandy, A study on the effect of process parameters on the joint strength and leak tightness in electromagnetically assisted adhesive Cu-SS tube-to-tube joining through statistical analysis, International Journal of Adhesion and Adhesives, Volume 116, 2022, 103136, https://doi.org/10.1016/j.ijadhadh.2022.103136
46. G. Abrahamson, J. Appl. Mech. Trans. ASME 28 (4) (1960) 519–528, cited By 42 https://doi.org/10.1115/1.3641777.
47. A. Bahrani, T. Black, B. Crossland, The mechanics of wave formation in explosive welding, Proc. R. Soc. Lond. A 296 (1445) (1967) 123–136.
48. J. Hunt, Philos. Mag. 17 (148) (1968) 669–680, cited By 55 https://doi.org/10.1080/ 14786436808223020.
49. G. Cowan, O. Bergmann, A. Holtzman, Metall. Mater. Trans. B 2 (11) (1971) 3145–3155, cited By 147 https://doi.org/10.1007/BF02814967.

Corresponding Author Email: kumar176103003@iitg.ac.in

50. J. Robinson, Philos. Mag. 31 (3) (1975) 587–597, cited By 38 https://doi.org/10.1080/14786437508226540.
51. D. Hay, Explosive welding: applications and techniques, High-Pressure Science and Technology, Springer 1979, pp. 1813–1836.
52. Wu, X., Shuai, J., Shan, K., Xu, K., and Di, Y. (July 7, 2020). "Hydraulic Burst Test of X52 Pipes With Defects or Nozzle Repair Structure." ASME. J. Pressure Vessel Technol. October 2020; 142(5): 054505. https://doi.org/10.1115/1.4047562
53. Nichit, Sudhir Kumar, et al. "Development of High Temperature Helium Leak Testing Facility for Front End of Nuclear Fuel Cycle." Anushaktinagar, Mumbai: Conference on Indigenous Nuclear Fuel programme in India-Achievements, Status and Prospects, 2019. 260-262.
54. Bahrani, A S, T J Black and B Crossland. "The Mechanics of Wave Formation in Explosive Welding." Proceedings of the Royal Society A: Mathematical, Physical, Engineering Sciences 296.1445 (1967): 123-136.
55. Shribman, Victor and Michael Blakely. "Benefits of the Magnetic Pulse Process for Welding Dissimilar Metals." Welding Journal 87.9 (2008): 56-59.

Preprint